Tools for the Advancement of Radiopharmaceutical Therapy

Mellhammar, Emma

2023

Document Version:
Publisher's PDF, also known as Version of record

Tools for the Advancement of Radiopharmaceutical Therapy

EMMA MELLHAMMAR
DEPARTMENT OF CLINICAL SCIENCES, LUND | FACULTY OF MEDICINE | LUND UNIVERSITY

Tools for the Advancement of Radiopharmaceutical Therapy

Tools for the Advancement of Radiopharmaceutical Therapy

Emma Mellhammar

LUND
UNIVERSITY

DOCTORAL DISSERTATION

Doctoral dissertation for the degree of Doctor of Philosophy (PhD) at the Faculty of Medicine at Lund University to be publicly defended on the 21 of April, 2023 at 09.00 in Torsten Landberg lecture hall, 3rd floor in the Radiotherapy building, Klinikgatan 5, Skåne University Hospital, Lund

Faculty opponent
Prof. Peter Bernhardt

Organization: LUND UNIVERSITY

Document name: DOCTORAL DISSERTATION **Date of issue:** 2023-04-21

Author(s): Emma Mellhammar **Sponsoring organization:**

Title and subtitle: Tools for the Advancement of Radiopharmaceutical Therapy

Abstract: Radiopharmaceutical therapy is used to treat cancers and other diseases with radiolabeled pharmaceuticals. The treatment targets specific cells, and the emitted ionizing radiation cause cytotoxic damage. Dosimetry is performed to estimate the absorbed dose from the energy deposited in the body. This requires measurement of the activity in vivo and knowledge of the retention time of the activity in tumor and organs. Preclinical trials precede clinical studies and evaluate the potential of new radiopharmaceuticals for treatment. Similarly, in vitro and in vivo experiments with radiopharmaceuticals and sources of ionizing radiation are performed to increase radiobiological knowledge, which is helpful in the optimization of radiopharmaceutical therapy. Dosimetry is also necessary for these studies to correctly quantify the biological response to ionizing radiation.

However, standard dosimetry only considers macroscopic volumes such as organs or solid tumors. Due to the short range of the emitted radiation, heterogeneous activity uptake can generate heterogeneous energy depositions. In a tumor, this means a large variation in particle tracks hitting the cell nuclei, where cells in undertreated areas will not receive any particle tracks through the cell nucleus. Since damage to DNA in the cell nucleus is the main cause of radiation-induced cell death, this can reduce the treatment effect. Early insight into these limitations of a new radiopharmaceutical can be achieved in preclinical studies investigating the intra-tumoral distribution of the radiopharmaceutical uptake. Paper 4 investigated the tumor control probability from the intra-tumoral distribution of 177Lu-PSMA-617 in LNCaP xenografts. Monte Carlo simulations can be used for small-scale and microscopic dosimetry, where small targets such as cells and cell nuclei are considered. Similarly, in paper 3, simulations of an alpha particle source and cell nuclei irradiated were used to estimate the distribution of induced γ-H2AX foci in PC3 cells irradiated with an 241Am source in vitro.

In preclinical studies of therapeutic radiopharmaceuticals, xenografted animal models are followed post-injection over long periods to evaluate the treatment response. This is usually done by measuring changes in tumor size over time. In addition, molecular imaging with positron emission tomography (PET) offers an opportunity to measure biochemical changes in vivo, such as the radiation damage response. However, as investigated in paper 1, gamma emission from the therapeutic radiopharmaceutical in the animal model can cause perturbations to the image by increasing dead-time losses and causing signal pile-up. However, as suggested in paper 2, preclinical intra-therapeutic PET imaging can still be performed during 177Lu-labeled radiopharmaceutical therapy, with shielding attenuating the excess photons while still allowing coincidence detection of annihilation photons. **Key words:** Radiopharmaceutical therapy, nuclear medicine, Monte Carlo simulation, Intratherapeutic preclinical PET, alpha particles, beta particles, radionuclides, radiobiology, γ-H2AX, dosimetry

Classification system and/or index terms (if any) Supplementary bibliographical information

Language: English **ISSN and key title**: 1652-8220 Lund University, Faculty of Medicine Doctoral Dissertation Series 2023:46

ISBN: 978-91-8021-386-8

Recipient's notes **Number of pages**: 93

Price Security classification

Signature  Date 2023-03-10

Tools for the Advancement of Radiopharmaceutical Therapy

Emma Mellhammar

LUND
UNIVERSITY

Coverphoto by Emma Mellhammar. Isotope Chart Embrodery.
Portrait of Marie Curie by Oskar Stålberg.

Faculty of Medicine
Department of Clinical sciences, Lund

ISBN 978-91-8021-386-8
ISSN 652-8220

Printed in Sweden by Media-Tryck, Lund University
Lund 2023

Media-Tryck is a Nordic Swan Ecolabel certified provider of printed material. Read more about our environmental work at www.mediatryck.lu.se
MADE IN SWEDEN

Dedicated to my mother, for love and knowledge.

Contents

Abstract

Radiopharmaceutical therapy is used to treat cancers and other diseases with radiolabeled pharmaceuticals. The treatment targets specific cells, and the emitted ionizing radiation cause cytotoxic damage. Dosimetry is performed to estimate the absorbed dose from the energy deposited in the body. This requires measurement of the activity in vivo and knowledge of the retention time of the activity in tumors and organs. Preclinical trials precede clinical studies and evaluate the potential of new radiopharmaceuticals for treatment. Similarly, in vitro and in vivo experiments with radiopharmaceuticals and sources of ionizing radiation are performed to increase radiobiological knowledge, which is helpful in the optimization of radiopharmaceutical therapy. Dosimetry is also necessary for these studies to correctly quantify the biological response to ionizing radiation.

However, standard dosimetry considers macroscopic volumes such as organs or solid tumors. Due to the short range of the emitted radiation, heterogeneous activity uptake can generate heterogeneous energy depositions. In a tumor, this means a large variation in particle tracks hitting the cell nuclei, where cells in undertreated areas will not receive any particle tracks through the cell nucleus. Since damage to DNA is the main cause of radiation-induced cell death, this can reduce the treatment effect. Early insight into these limitations of a new radiopharmaceutical can be achieved in preclinical studies investigating the intra-tumoral distribution of the radiopharmaceutical uptake. Paper 4 investigated the tumor control probability from the intra-tumoral distribution of ^{177}Lu-PSMA-617 in LNCaP xenografts. Monte Carlo simulations can be used for small-scale and microscopic dosimetry, where small targets such as cells and cell nuclei are considered. Similarly, in paper 3, simulations of an alpha particle source and cell nuclei were used to estimate the distribution of induced γ-H2AX foci in PC3 cells irradiated in vitro with an ^{241}Am source.

In preclinical studies of therapeutic radiopharmaceuticals, xenografted animal models are followed post-injection over long periods to evaluate the treatment response. This is usually done by measuring changes in tumor size over time. In addition, molecular imaging with positron emission tomography (PET) offers an opportunity to measure biochemical changes in vivo, such as the radiation damage response. However, as investigated in paper 1, gamma emission from the therapeutic radiopharmaceutical in the animal model can cause perturbations to the image by increasing dead-time losses and causing signal pile-up. As suggested in paper 2, preclinical intra-therapeutic PET imaging can still be performed during ^{177}Lu-labeled radiopharmaceutical therapy, with shielding attenuating the excess photons while still allowing coincidence detection of annihilation photons.

Populärvetenskaplig sammanfattning

Radionuklidterapi används för att behandla cancer och andra sjukdomar. Radioaktiva läkemedel, så kallade radiofarmaka, målsöker specifika sjuka celler i kroppen och sänder ut joniserande strålning som orsakar celldöd. Därmed kan de behandla en sjuk volym i kroppen, så som en tumör. Radionuklidterapi är en form av strålbehandling, men strålkällan fördelas inuti kroppen, i stället för att stråla på kroppen utifrån. Radionuklidterapi kan även behandla cancermetastaser, dvs tumörer som har spritt sig i kroppen från den primära tumören. Detta har potential att leda till förbättrad behandling av cancerdiagnoser som idag har väldigt dålig prognos.

Radiofarmaka administreras vanligtvis med en intravenös injektion, vartefter det cirkulerar runt i blodomloppet och med tiden tas upp av de målsökta cellerna, eller renas ur blodet via kroppens reningsvägar, så som via njurarna eller levern. Därför utsätts även friska organ och vävnader för strålning. Detta begränsar hur mycket radioaktivitet som kan administreras till en patient för att denna inte ska få allvarliga stålningsinducerade biverkningar eller skador. De radionuklider som används för terapi har långa halveringstider. Det som tas upp i kroppen blir därför kvar länge och deponerar långsamt sin strålning. Med hjälp av dosimetri beräknas den absorberade dosen från den deponerade strålningsenergin till både frisk och sjuk vävnad. Detta används för att förutsäja den förväntade effekten av strålningen. För att beräkna den absorberade dosen krävs att man mäter aktivitetsfördelningen i kroppen över tid.

När man utvecklar nya radiofarmaka utför man prekliniska studier i djurmodeller innan läkemedlet testas i människor. Dessa djur kan bära tumörer som behandlas av läkemedlet och behandlingseffekten kan följas över tid. För att studera biokemiska signaler inuti kroppen kan preklinisk positronemissionstomografi (PET) användas. På så sätt kan strålningseffekten studeras både tidigt och sent under behandlingen. Dock uppstår problem om höga aktiviteter av ett radiofarmaka finns i djurets kropp. Detta kan introducera brus och signalförlust i PET-bilden och medför att de kvantitativa egenskaperna sätts ur spel. Problemet kan dock avhjälpas om strålningen från den terapeutiska radionukliden skärmas.

Även i prekliniska försök är det viktigt att beräkna den absorberade dosen för att utvärdera behandlingseffekten. Likaså är det viktigt att göra dosimetriska beräkningar när man utför radiobiologiska försök på celler eller djur som syftar till att förklara de biologiska processer som sker när celler och vävnader utsätts för joniserande strålning. De dosimetriska metoder som används i dag tar hänsyn till makroskopiska volymer, så som hela organ. Strålning som sänds ut från radiofarmaka för radionuklidterapi har en kort räckvidd. Vid heterogen fördelning av ett radiofarmaka i en tumör, kan även den

absorberade dosen i volymen bli ojämn. Celler i delar av tumören som tagit upp mindre radioaktivitet riskerar att bli underbehandlade. För att uppskatta denna varians måste dosimetriska metoder som tar hänsyn till strålningens räckvidd och som beräknar absorberad dos till små volymer, så som celler och cellkärnor, användas. Med matematiska modeller av celler och tumörer kan simuleringar av den fysikaliska växelverkan mellan joniserande strålning och vävnad användas för att beräkna denna småskaliga dosimetri.

Preface

The work included in this thesis began in the spring of 2015 in the Systemic therapy group at the Faculty of Medicine in Lund. The aim initially took a broad scope and intended to develop dosimetry tools for radiopharmaceutical therapy in preclinical trials. At the time, the principal supervisor of the thesis was an expert in optical imaging and mainly focused on Cherenkov emission imaging (CEI). The intention was to expand on the potential of CEI as a tool to follow the treatment outcome of xenografts in small animal models when treated with radiopharmaceutical therapy and to examine its potential to estimate the absorbed dose of the treatment. However, as the principal supervisor unfortunately chose to leave his academic career, the position was filled by one of the co-supervisors. With his lifelong career in Medical Physics, the shoes were undoubtedly filled, but with slightly different expertise. The study plan, therefore, needed a more extensive revision to fit the available knowledge and assets of the reshaped research group.

By expanding the use of Monte Carlo simulations in the GATE environment and taking in the essential aspects of small-scale dosimetry in radiopharmaceutical therapy, the thesis has been shaped around the interplay between theoretical modeling and laboratory and preclinical work.

Another hiccup in work with this thesis was the loss of access to an antibody we originally planned to label as a PET tracer. As the antibody targeted a specific epitope on prostate cancer cells, it could not easily be replaced, and the planned study had to be canceled.

While not as initially intended, this thesis has allowed exploration of the limitations of radiopharmaceutical therapy and dosimetry. From the projects included, initial naïve intentions have been tested and rebuked. The sometimes overwhelming complexity of laboratory and preclinical work has humbled this doctorate student and reshaped her way of forming new hypotheses. Rather than assuming a multiplicative gain when combining different techniques, a restrictive attitude toward the combination of modalities has arisen. As each new method demands an in-depth understanding of its strength, weaknesses, and limitations, errors are swiftly introduced and missed when ambition rules over skepticism.

With these experiences, new ideas are shaped with more care, with lessons learned from failure and growth.

List of Publications

Paper I: Counting Rate Characteristics and Image Distortion in Preclinical PET Imaging During Radiopharmaceutical Therapy

Mellhammar E, Dahlbom M, Axelsson J, Strand SE.

Journal of Nuclear Medicine. 2016. 57(12):1964-1970.

Paper II: Preserving Preclinical PET Quality During Intratherapeutic Imaging in Radionuclide Therapy with Rose Metal Shielding Reducing Photon Flux.

Mellhammar E, Dahlbom M, Evans-Axelsson S, Strand SE.

Journal Nuclear Medicine. 2019. 60(5):710-715.

Paper III: Small-scale dosimetry for alpha particle ^{241}Am source cell irradiation and estimation of γ-H2AX foci distribution in prostate cancer cell line PC3

Mellhammar E, Dahlbom M, Vilhelmsson Timmermand O, Strand SE.

EJNMMI Physics. 2022. 9, 46

Paper IV: Tumor Control Probability based on small-scale Monte Carlo Dosimetry model - calculating necessary activity to administrate in radionuclide therapy for heterogeneous intra-tumoral activity uptake

Mellhammar E, Dahlbom M, Vilhelmsson Timmermand O, Strand SE.

Submitted to Journal of Nuclear Medicine January 2023 and currently under review.

Author's contribution to the papers

Paper I

My supervisors suggested the principal idea, but I participated in the study design development. I performed, with help, all experiments and data collection. I performed the main part of the data analysis and presentation of the results, drafted the manuscript, and was the main and corresponding author.

Paper II

This study was related to paper 1, and my supervisors suggested the principal idea of metal shields. I contributed to the study design, overseeing the design and casting of the shields. I performed, with help, all experiments and data collection. I performed the Monte Carlo simulations, optimized the digitizer model, and handled the data output. I performed the data analysis, drafted the manuscript, and was the main and corresponding author.

Paper III

I suggested the principal idea of the study and its design. I performed, with help, the cell work and cell irradiations. I performed cell staining, confocal microscopy imaging, and image analysis to detect fluorescent foci. I built the Monte Carlo simulation model and analyzed the resulting data. I drafted the manuscript and was the main and corresponding author.

Paper IV

I suggested the principal idea of the study and its design. The main work with the animal model was performed by others. I performed, with help, the cryo-sectioning and autoradiography measurements. I performed the image analysis of the histological stains to calculate the cell density map. I built the Monte Carlo simulation and performed all data analysis. I drafted the manuscript and was the main and corresponding author.

Abbreviations

2D, 3D	two- and three-dimensional
AUC	area under the curve
CEI	Cherenkov emission imaging
CT	computed tomography
DAPI	fluorescent DNA stain (4′,6-diamidino-2-phenylindole)
DAR	digital autoradiography
DDR	DNA damage response
DNA	deoxyribonucleic acid
DSB	double-strand break
EBRT	external beam radiotherapy
FWHM	full width at half maximum
GPS	general-purpose source
H2AX	H2A histone X
HE	hematoxylin and eosin
HR	homologous recombination
IAEA	International Atomic Energy Agency
ICRU	International Commission on Radiation Units and Measurements
LET	linear energy transfer
LOR	line of response
LQ	linear quadratic
MIRD	Medical Internal Radiation Dose
NET	neuroendocrine tumors
NHEJ	non-homologous end joining
OAR	organ at risk
PDF	probability density function
PET	positron emission tomography
PRRT	peptide receptor radionuclide therapy
PSMA	prostate specific membrane antigen
RBE	relative biological effectiveness
RIF	radiation-induced focus
RPT	radiopharmaceutical therapy
SF	surviving fraction
SP	surviving portion
SPECT	single photon emission computed tomography
SSB	single-strand break
TCP	tumor control probability

1 Introduction

Radiopharmaceutical therapy (RPT) is the use of radionuclides, unlabeled or conjugated to a carrier, aimed to target specific lesions. Ionizing radiation emitted from the radionuclides by radioactive decay interacts in matter and deposits energy, causing lethal damage to the targeted cells. Since radiopharmaceuticals are delivered systemically, they can reach targets unavailable by surgery or other interventions. It is a form of radiotherapy but differs fundamentally from external beam radiotherapy (EBRT). By comparison, during EBRT, the ionizing radiation is delivered where the beam is aimed. The radiation field is collimated to limit unnecessary exposure, and the absorbed dose can be "painted" to the shape of a target volume by intensity-modulated radiation therapy. The treatment is, in most cases, delivered in daily fractions over several weeks. Once the beam is turned off, the high dose rate radiation ceases. This is in contrast to RPT, where the injected radiopharmaceutical can remain present in the body over several weeks or months. It can distribute throughout the entire body and is slowly removed by radioactive decay and biological clearance. The low dose rate, therefore, changes over time until no longer present or irrelevant in any biological sense.

RPT can potentially treat metastatic disease spread from the primary tumor to distant parts of the body if available through the path of delivery. This brings hope for treatments for patients with very poor prognoses. Hypothetically, it also means reducing the recurrence of treated cancers, as microscopic metastases undetected by current diagnostic tools may also receive the treatment, preventing them from slowly growing into new tumors. In some respects, RPT, therefore, has more in common with immunotherapy or chemotherapy. However, the actual damage to the lesions is caused by the emitted ionizing radiation. As such, it is non-selective and can damage cells with or without targeted epitopes as long as they are within its range. This can either be an advantage, as radiation can reach within a tumor with poor penetration of the radiopharmaceutical or a disadvantage if it reaches healthy neighboring tissues.

Like EBRT, RPT is limited by the inevitable delivery of ionizing radiation to healthy tissues. While these organs at risk (OAR) are located in the beam path for EBRT, in RPT, they are commonly organs through which the radiopharmaceutical is cleared from the body, such as the liver and kidneys, or normal uptake in organs such as the

salivary glands. In immuno-RPT, the bone marrow can receive a substantial absorbed dose. To avoid severe side effects, dosimetry for the OARs should be performed to calculate the maximum activity that can be administrated without unacceptable side effects.

Increasing the therapeutic effect of the administrated activity requires the adjustment of several biochemical parameters. If it is possible to increase the specificity to the targeted epitope, improve its tumor penetration, reduce the bloodstream circulation time, and avoid re-release of the radionuclide to the bloodstream once taken up, more of the ionizing radiation can be delivered where best suited. Having these perspectives in mind in preclinical trials of new radiopharmaceuticals could improve the success of those later investigated in clinical trials.

Evaluating the dose-effect relationship of the emitted ionizing radiation requires dosimetry. While a well-integrated part of EBRT, RPT still struggles with practical implementations of radiation dosimetry to optimize clinical treatments (*1*). However, recent efforts have been made, such as the International Commission on Radiation Units and Measurements (ICRU) report on *Dosimetry-Guided Radiopharmaceutical Therapy* (*1*). Similarly, the IAEA report *Guidance for preclinical studies with radiopharmaceuticals* emphasizes the importance of dosimetry and the need to consider the short range of alpha particles and low energy electrons in small-scale dosimetry models (*2*).

Dosimetry models are necessary as the absorbed dose cannot be directly measured during therapy. Lack of detail of the activity distribution or target volume can mischaracterize the dose-effect relationship. However, data necessary for improved dosimetry and evaluation of the radiobiological response is more available in preclinical trials compared to clinical. Utilizing this has the potential to enhance the development of new radiopharmaceuticals. For example, the uptake of a radiopharmaceutical intratumorally or inside an organ can be investigated in detail, and the biodistribution can be followed more closely in vivo and ex vivo. This can make preclinical trials more effective and increase the chance of translating new radiopharmaceuticals to clinical use, favoring future patients.

1.1 Aim of this thesis

This thesis aims to investigate tools that can improve in vitro and preclinical in vivo dosimetry and treatment response imaging of RPT. The results will hopefully suggest methods and applications that increase the chances of successful translation of new

therapeutic radiopharmaceuticals from preclinical trials to clinical use. To accomplish this, models have been built from the experimental results.

The included projects investigate the limits of intratherapeutic PET imaging and the necessity of small-scale and microdosimetry for radiation emitted from therapeutic radiopharmaceuticals. Monte Carlo simulations are used in three of the four papers; to simulate a preclinical PET system and the radiation emitted by radionuclides in the camera, to investigate the absorbed dose to cells irradiated with alpha particle radiation, and to build a tumor dosimetry model for the calculation of tumor control probability.

Specifically, the aims of the individual projects are as listed:

1. To investigate the limits of intra-therapeutical PET-imaging when treating small animal models with high therapeutic activities of for example ^{177}Lu.
2. To explain the cause of signal-loss in intra-therapeutical PET imaging through Monte Carlo simulations and investigate the recovered image quality when performed with Rose metal shielding.
3. To construct a Monte Carlo simulation model of an alpha particle cell irradiator and investigate the cell nucleus hit distribution. Then, to compare the results from this small-scale dosimetry model to the distribution of γ-H2AX foci detected in PC3 cells irradiated with the physical alpha irradiator.
4. To investigate the tumor control probability in tumors with heterogeneous intra-tumoral activity uptake by simulating the tumor absorbed dose distribution for radionuclides emitting short- and long-range radiation. Also, to investigate the opportunity to estimate the necessary injected activity to achieve tumor control.

2 Background

Not much time passed between the discovery of radium by Marie and Pierre Curie in 1898 and the first attempts to use it for medical applications. Many fashionable products of the time added radium to their formula to sell the promise of the newly discovered rays, sometimes with deadly outcomes (*3,4*). Still, serious researchers identified the true healing potential of the radionuclide and investigated ways to utilize it. The first efforts to treat cancer with an alpha emitter were performed at the beginning of the last century. Radium salts could be loaded into applicators and placed close to a superficial abnormal growth for local treatment. This was the beginning of brachytherapy.

After the discovery of isotopes by Joseph J. Thomson, having been suggested to exist by Frederick Soddy in 1913, the discovery of more artificially produced radionuclides took off in the 1930s. In 1938, iodine-131 (^{131}I) was discovered, and quickly diagnostic applications were established. In the 1940s, treatments of hyperthyroidism and thyroid cancer with ^{131}I were performed. In the 1970s, indium-111 (^{111}In) chelates enabled targeting tumors labeled with monoclonal antibodies and later led to ^{131}I-labelled monoclonal antibodies for treating malignant melanoma. In the 1990s, the first peptide receptor radionuclide therapy (PRRT) for neuroendocrine tumors (NETs) with ^{111}In-pentetreotide in patients was performed. These synthetic somatostatin analogs binding to the somatostatin receptors expressed by NETs have since been labeled to the beta-emitting radionuclides yttrium-90 (^{90}Y) and lutetium-177 (^{177}Lu).

Today, several radiopharmaceuticals are routinely used clinically, and others are under development. (^{131}I)-sodium iodine remains one of the most commonly used radiopharmaceuticals, offering curative treatment of thyroid cancer and hyperthyroidism (*1*). In 2013, radium-223 dichloride ($^{223}RaCl_2$) was approved for clinical palliative treatment of patients with bone metastasis from castrate-resistant prostate cancer (*1*). It reduces abnormal bone growth and slightly improves overall survival (*5,6*). ^{177}Lu-labeled peptides are used to treat neuroendocrine tumors (NETs) (*7*). Prostate specific membrane antigen (PSMA) can be targeted with ligands or antibodies labeled with ^{177}Lu, or alpha emitters such as actinium-225 (^{225}Ac) or thorium-227 (^{227}Th) (*8-10*). Recently, ^{177}Lu vipivotid tetraxetan, previously known

under the name ^{177}Lu-PSMA-617, was approved by the FDA, and soon after by the European Medicines Agency (*11*). ^{90}Y microsphere radioembolic therapy, although not a systemic RPT treatment, is used for treating hepatic malignancies. Studies of these ^{90}Y treatments have contributed to the slowly growing pool of evidence for the usefulness of patient dosimetry in RPT (*1*).

The primary tool for estimating the risks and benefits of ionizing radiation, the *absorbed dose*, is a quantity available through models and approximations. It is not directly measured in vivo but estimated from measurements of the activity, supported by measurements in phantoms and simulations. Today, most therapeutic radiopharmaceuticals are administrated as a standardized activity, with little or no regard to the tumor burden, biokinetics, target expression, etc., of individual patients. As a result, the absorbed dose to the target volume or OARs can vary significantly between patients. Similarly, the treatment response in preclinical trials is commonly related to injected activity and not to the absorbed dose in the target volume (*12*).

To advance RPT, improved dosimetry is necessary to enable individualized therapy. In addition, dosimetry models in preclinical trials can facilitate the development of new radiopharmaceuticals and are necessary to quantify radiobiological phenomena.

2.1 Interaction of radiation with matter

Radionuclides are atoms with an unstable nuclear composition that can lead to a transformation of the nucleus and a release of energy as ionizing radiation. For RPT, radionuclides emitting alpha particles, beta particles, or Auger electrons, all examples of charged particles, are of interest. Many of these also emit photons that sometimes are utilized for imaging and internal localization and quantification of the therapeutic radionuclide. For diagnostic imaging in nuclear medicine, photon-emitting radionuclides are used, although the photons detected in PET imaging appear after the emitted positron annihilates with an electron.

Ionizing radiation can cause secondary release of particles, most relevantly electrons, through interactions with matter (*13*). This energy transfer can cause biological damage to molecular structures, such as the DNA molecule.

When passing through matter, charged particles most commonly interact directly through inelastic collisions with electrons in the atomic shells. Energy from the primary charged particle is then transferred to the electron, receiving enough energy to escape its bound state. If the transferred energy is high enough, the released electron can interact and cause further release of electrons, often referred to as delta-particles (*14*).

The interaction of a charged particle causes tracks of multiple interactions. These can be characterized by numerous points and clusters of interactions, delta-particles, and points of angular changes.

Photons are indirectly ionizing, passing their energy to charged particles that, in turn, can cause further ionizations. The probability for specific interactions is energy dependent, and in the energy interval relevant for nuclear medicine, photon absorption, Compton scattering, coherent scattering, and pair production are relevant (*14*). The attenuation of photons can be described by the *mass attenuation coefficient* $\frac{\mu}{\rho}$, where the contribution of each interaction is summed in the *linear attenuation coefficient,* μ, for the density of the material ρ. The mass attenuation coefficient depends on the atomic composition of the material for a given photon energy. The reduced photon rate $N(x)$ of the initial photon rate N_0 traveling the distance x in a material with the mass-thickness $\rho \cdot x$ (kg/m^2) can then be calculated as

$$N(x) = N_0 \cdot e^{-\frac{\mu}{\rho}\rho \cdot x} \tag{2.1}$$

To estimate the biological effect of ionizing radiation, the *energy deposit* from every interaction is summed as the *energy imparted* to matter in a volume. The *absorbed dose* (*1*) is then defined as the mean energy imparted $d\bar{\varepsilon}$ by ionizing radiation per mass element dm

$$D = \frac{d\bar{\varepsilon}}{dm} \tag{2.2}$$

Its unit gray (Gy) is defined as joule per kilo (J/kg). Previously the unit "rad" was used as a measure of radiation exposure, also defined as energy deposited per unit mass, and 1 Gy equals 100 rads. The absorbed dose is used to quantify acute radiation response or probability of stochastic radiation effects. In RPT, radiopharmaceuticals are administrated with the intention to deliver high absorbed doses in targeted volumes. With dosimetry, the absorbed dose is measured or calculated.

2.2 Radiobiology

Following the discovery of x-rays by Wilhelm Conrad Röntgen, ionizing radiation quickly found its home in the medical clinic. New promising applications in diagnostics and therapeutics emerged, but also the realization of its potential dangers. Understanding of the harmful effects would not appear until the discovery of the DNA

molecule. However, both acute and long-term effects of radiation exposure, such as skin burns and the induction of cancer, were noticed in early investigations. Researchers also realized ionizing radiation could affect the genomic material, as hereditary effects were observed in irradiated animals, for example, flies (*15,16*).

To explain radiobiological effects, a useful property of ionizing radiation is its linear energy transfer (LET), defined as:

$$LET = \frac{dE}{dl} \tag{2.3}$$

where LET is the mean energy absorbed by matter dE per unit length dl of the radiation track by charged particles (*1*). It is relevant for directly ionizing radiation, such as the alpha particles, beta particles, and Auger electrons utilized in RPT. Sometimes LET is defined for photons and neutrons but refers then to the secondary electrons produced during interactions in matter. As LET increases, ionizations along the track appear more densely, and the likelihood of damage on the DNA strand increases, as illustrated in Figure 2.1.

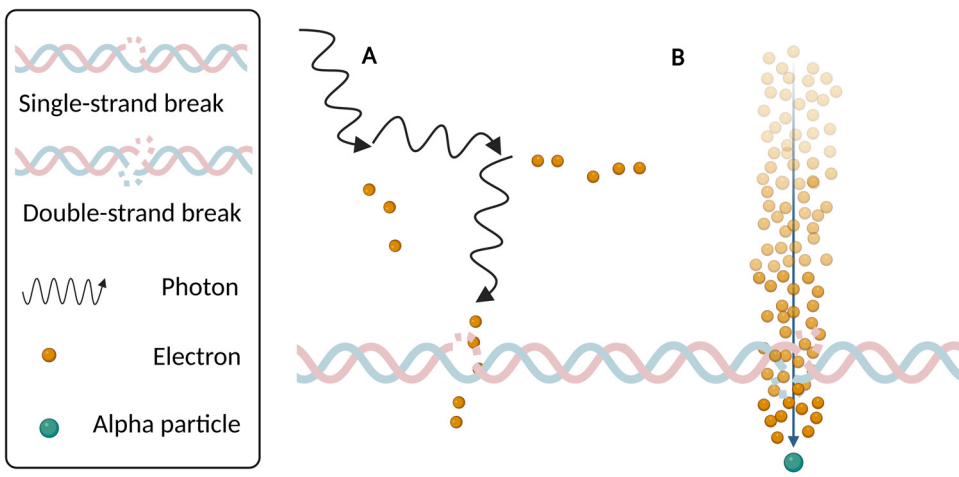

Figure 2.1 Interaction of photons with matter, generating sparse tracks of ionizations and secondary electrons (A), and interaction of an alpha particle with matter, generating dense tracks of ionizations (B). Photons and electrons are examples of low LET, mainly causing single-strand breaks on DNA, while alpha particles are an example of high LET radiation, mainly causing double-strand breaks on DNA. Created with BioRender.com.

High LET radiation has a higher relative biological effectiveness (RBE) since an equal absorbed dose of low and high LET radiation may not cause the same damage or

biological response. Low LET radiation (Figure 2.1 A), such as x-rays and electrons, mainly cause DNA damage through indirect action. Since the likelihood of direct ionization on the DNA molecule is low, most interactions occur with other abundant molecules in the radiated volume, primarily water molecules. Through further reactive steps, free radicals are produced. These have unpaired electrons that make them very reactive. If they are close enough to the DNA molecule, they can diffuse the short distance and cause damage through oxidative reactions. In contrast, high LET radiation mainly causes damage through direct action since it produces many ionizations along its tracks that can interact directly with the DNA molecule (Figure 2.1 B).

Ionizing radiation can cause multiple types of damage, including single-strand breaks (SSB), double-strand breaks (DSB), and base damage. SSB consist of a single break in the helix sugar-phosphate backbone. Although SSB can be produced in high numbers by low LET ionizing radiation (Figure 2.1 A), these do not pose a high risk for cell death or mutations. Since the cell can use the complementing strand as a blueprint, they are easily repaired. DSBs are breaks on both strands on either side of the helix within a distance of a few base pairs. Unrepaired DSBs (Figure 2.1 B) can lead to cell death. Also, mis-repaired DSB can cause chromosomal aberrations, mutations, and cell death.

2.2.1 DNA repair

DNA damage can be repaired through multiple repair pathways. For radiation-induced damage, a few pathways affect the outcome of the exposure. Schematically, DNA damage response (DDR) can be described as a chain of events involving the initial damage sensing, the transduction of a signal to recruit effector proteins, the transcription of other necessary factors, initiation of cell cycle arrest, and possibly the initiation of apoptosis.

DNA damage is detected by sensor proteins continuously checking the genome for damage. To initiate repair, cell death, and cell cycle arrest, signaling proteins modify themselves or other recruited proteins, predominantly through phosphorylation or acetylation. This can function as a marker at the damage point on the chromatin. Noteworthy is the phosphorylation of checkpoint kinase 2 (CHK2) to initiate cell-cycle arrest pathways, tumor protein p53, an initial step of apoptosis pathways, and H2A histone X (H2AX), which amplifies the damage signal. As discussed later, after irradiation, the phosphorylated form of H2AX, γ-H2AX, is a molecular target for DSB.

Radiation-induced DSBs can be repaired through homologous recombination (HR) or non-homologous end joining (NHEJ). Loss of either of these pathways by mutations

can lead to an increased radiosensitivity. HR is an almost error-free pathway for DSB repair since it uses the sister chromatid as a template to rebuild the strands. However, it is only available in the later phases of the cell cycle, after transcription, when the genome has been doubled. The NHEJ pathway is available throughout the cell cycle but is much less accurate than HR as it simply tries to join together the loose DNA strand ends.

2.2.2 Cell survival models

While the interaction of radiation and induction of damage happens within a short time frame, cell death, tissue damage, or tumor response is comparatively slow. Long-term stochastic effects are even slower, appearing years or decades after the irradiation that caused the initial damage. To build models predictive of therapeutic outcomes, it is necessary to quantify cell death. Usually, this means losing the ability to proliferate, as these cells will not contribute to further tumor growth. The standard method for measuring this is called the clonogenic (or colony-forming) assay (*17*). Cells are seeded sparsely, either before or directly after irradiation. Those with an intact proliferative ability will form colonies, typically after 1-2 weeks.

When investigating the radiosensitivity of cells in vitro, the surviving fraction (SF) as a function of absorbed dose is measured. The SF is most often visualized on a semi-logarithmic scale. Then, the curve usually has an initial shoulder that turns into a slope at higher absorbed doses. The underlying biological reasons for this shape have not been simple to explain. The probability of a radiation interaction is random and can be approximated by a Poisson distribution, and an exponential decrease in survival is expected. The shoulder width depends on factors such as the cells' ability to repair damage and the function of cell cycle checkpoints.

Early models tried to give a functional explanation to the SF curve shape, such as the target models (*18*). They assumed all cells contained one or several targets that needed to be inactivated for the cell to die. However, they were never entirely successful in predicting the SF over the range of relevant absorbed doses. The most successful model for clinical applications is the linear quadratic model (LQ model) (*19*).

$$SF = e^{-\alpha D - \beta D^2} \tag{2.4}$$

Here, the survival (SF) is an exponential function of absorbed dose (D) with two fitting parameters (α and β) describing the impact of a linear and a quadratic term of absorbed dose. It is a quasi-empirical model since it does not explain the parameters

mechanistically. But the general good fit of the model has led to attempts of finding an underlying biological base for the model's success (*19*).

2.2.3 Radiobiology in radiopharmaceutical therapy

EBRT and PRT differ in many radiobiological aspects. RPT radiopharmaceuticals emit moderate to high LET particles with the potential to cause multiple DSBs from a single radiation track. Therefore, they can be effective tumor killers if taken up with high tumor specificity. The limited range of high LET radiation, such as alpha particles and Auger electrons, makes factors such as internalization and proximity to the cell nucleus relevant for the biological outcome (*20*). Also, since they cause more lethal damage, repair of sub-lethal damage and dose rate is less critical. In general, alpha RPT does not seem to be affected by therapy resistance (*20,21*).

However, the dose rate in a tumor during RPT is much lower than in EBRT and varies over time, first due to the initial uptake and later due to the physical decay and excretion of the radionuclide from the tumor. It is unclear if damage repair pathways will perform differently under these conditions. The radiosensitivity, investigated by the clonogenic assay, is often measured after high dose-rate irradiations, even for high LET radiation. The alpha-emitting americium-241 (^{241}Am) source used in paper 3 has a much higher dose rate than the expected intra-tumoral dose rate during alpha-RPT. Applying radiosensitivity measured under these conditions to dosimetry models for RPT is questionable.

2.3 Cell cultures and preclinical tumor models

Cancer cell lines can be established from patient biopsies. Under the right circumstances, although not clearly understood (*22*), these cells can become a continuously growing and dividing cell line that offers an in vitro model of cancer cell characteristics. In paper 3, the prostate cancer cell line PC3 (*23*) is grown and irradiated with alpha particles in vitro. In paper 4, mice inoculated with the prostate cancer cell line LNCaP (*24*) on the flank to generate xenograft tumors are used to evaluate the intra-tumoral ^{177}Lu-PSMA-617 uptake.

Cell culture experiments are comparatively easy to perform and can be used to assess the radiosensitivity of a cancer cell line, usually by the colony-forming assay (*17*). Cultured cells can grow faster than tumor models, and much data can be collected quickly. However, irradiating cells in vitro with radiopharmaceuticals is not always a

straightforward procedure, and how to perform dosimetry must be considered carefully, as discussed further in chapter 5.2.

The cellular response to radiation can be measured with multiple molecular techniques, both in vitro and in vivo. For example, there are many assays to measure DNA damage response signaling (*25*). Immunocytochemical methods can target specific antigens expressed by cells, such as proteins expressed in the DDR pathways or specific receptors on the cell surface. In paper 3, γ-H2AX, a histone phosphorylated early in the DDR to DSBs, is targeted by fluorescent immunohistochemistry in alpha-particle irradiated PC3 cells and imaged with fluorescence confocal microscopy.

In vivo experiments with xenografted animal models offer an opportunity to test the radiopharmaceutical systemically. Although the models might have a limited ability to imitate realistic cancer growth (*26*), they provide a model of the tumor microenvironment, as seen in a patient. Tumor growth can be followed over time, and the animal's blood values, weight, and overall health can be monitored. Similarly, in vitro and in vivo experiments are also used for basic radiobiological investigations (*16*).

With preclinical molecular imaging, the in vivo distribution of the radiopharmaceutical can be imaged for activity quantification in tumor volumes or OARs. Or, a diagnostic radiotracer can be used for functional imaging. An advantage of preclinical imaging is the opportunity to do repeated studies of the same animal over time. In these longitudinal studies tumor growth or regression, expression of a specific target or function can be followed over time (*27*). For example, our group performed ^{99m}Tc-MAG3 imaging studies of the kidneys after administration of high activity levels of ^{177}Lu-PSMA-617 (*28*) to investigate kidney damage and could see a significant change in function three months post-injection of the therapeutic radiopharmaceutical.

In vitro and preclinical trials with animal models are initial methods for clinical translation when developing new radiopharmaceuticals. In vitro cell studies assess characteristics such as molecular targeting and metabolic stability, while in vivo experiments evaluate biodistribution, pharmacokinetics, and toxicity (*29*). Promising compounds can be assessed by in vivo experiments in animal models that imitate the disease the radiopharmaceutical aims to treat. For RPT development, this typically means animals with xenografted tumors. These studies investigate if the radiopharmaceutical has a high tumor specificity, generates a therapeutic effect, and if there is increased accumulation in normal tissue, limiting the therapeutic window (*30*).

The goal of preclinical in vivo trials for non-radioactive therapeutic drugs differs from trials of therapeutic radiopharmaceuticals. They aim to detect the drug's biological response and adverse side effects. For therapeutic radiopharmaceuticals, it is most relevant to investigate whereto it will distribute in the body to assess where it could

cause a radiation response (*31*). For that reason, it is necessary to investigate the biodistribution of a radiopharmaceutical, or more precisely, the radionuclide. The spatial and temporal redistribution of the radiopharmaceutical after administration (most often by intravenous injection) determines where energy from the emitted radiation will be deposited in the body and, subsequently, the resulting absorbed dose. The dispersion and relocation of the radiopharmaceutical determines the biokinetics. As intended, the targeted cell epitope can specifically take up the radiopharmaceutical. However, there is a risk that it will later disassociate from the receptor and relocate elsewhere. There is also a possibility of disassociation between the radionuclide and the carrier molecule (*30*). The biokinetics of the free radionuclide may be very different from the radiopharmaceutical, and risks accumulating in radiosensitive normal tissues. Much of the injected radiopharmaceutical will remain in the blood pool and be cleared by kidneys or liver (*29*). This is why these organs are often OARs during RPT.

After sacrificing and dissecting the animals, the tumor environment and normal tissues can be investigated on a detailed scale. The biodistribution at the time of sacrifice can be analyzed by measuring the activity in harvested organs and tissues in a well counter, establishing the ratio of injected activity per mass (%IA/g) for each organ. The biodistribution is an essential step in dosimetry calculations for in vivo experiments; therefore, necessary if the treatment outcome is to be evaluated by the absorbed dose (*2*). In addition, the internal activity distribution can be investigated in thin sections of tissue imaged by autoradiography. This can reveal heterogeneity of the activity distribution, leading to large variances in absorbed dose across the tumor volume for short-ranged emissions such as alpha particles. This is preferably combined with histological staining, where multiple receptors and expressions can be evaluated. For RPTs, tumor necrosis, proliferation, and the specific epitope targeted by the therapeutic radiopharmaceutical can be visualized in tissue sections. For improved sensitivity, fluorescent markers can be used instead of chromatic stains and are then imaged with fluorescence microscopy.

3 Imaging in nuclear medicine

Radionuclides used in diagnostic nuclear medicine emit photons with high enough energy to escape the body before being attenuated. This enables detection outside the patient or, for preclinical applications, the animal model. Some radionuclides used for therapy also have, in contribution to their emission of alpha particles, beta particles, or Auger electrons, some emission of photons of sufficiently high energies. A good example is ^{131}I, which through beta decay, emits beta particles well suited for therapeutic applications but also emits photons, most notably one of 364 keV (81.5 %), that can be detected by gamma or SPECT cameras. Therefore, imaging of radionuclides in vivo is used both for diagnostic applications and as a tool for dosimetry during radiopharmaceutical therapy. Imaging in nuclear medicine aims to detect the radiopharmaceutical inside the body, in an organ, or tissue after its administration. SPECT and PET imaging can be used quantitatively to determine the activity inside a delineated volume.

3.1 Photon detection for nuclear medicine imaging

Imaging in nuclear medicine gained momentum with the Anger camera, (*32*) now commonly referred to as a scintillation camera or a gamma camera (*33*). From the initial planar images, the technique evolved into single photon emission computed tomography (SPECT) and positron emission tomography (PET). SPECT and PET are commonly integrated with an x-ray computed tomography (CT) system. Combined imaging offers an anatomical reference for the functional nuclear image and a source for attenuation correction of the nuclear image.

Detection of photons is possible with many kinds of detectors. For imaging in nuclear medicine, scintillator crystals and solid-state detectors are primarily used (*34*). To generate an image of the internal activity distribution from the detected interactions in the detector volume, the detector must be capable of analyzing both the direction and the energy of the photons. Photons interacting in the detector volumes will deposit some or all their energy, generating a flash of visible light if inside a scintillator or an

electron-hole pair in a solid-state detector. In either case, the signal is collected and transformed into an electrical signal, then processed to decide the energy deposited and sometimes the timing of the event. Knowing the energy is necessary to determine if the photon follows its initial trajectory or has scattered before reaching the detector. If so, it has lost some of its energy and changed its direction. The information of the initial trajectory is then lost, and the event will not contribute constructively to the image quality but instead introduce noise, lowering the image contrast.

Scattered photons can be excluded by only considering photons depositing enough energy to fall within an energy window. However, the finite energy resolution of the detectors limits the system's ability to reject scattered events using energy discrimination. As a result, some scattered photons will inevitably be included in the image data and degrade the image quality and the quantitative abilities of the camera.

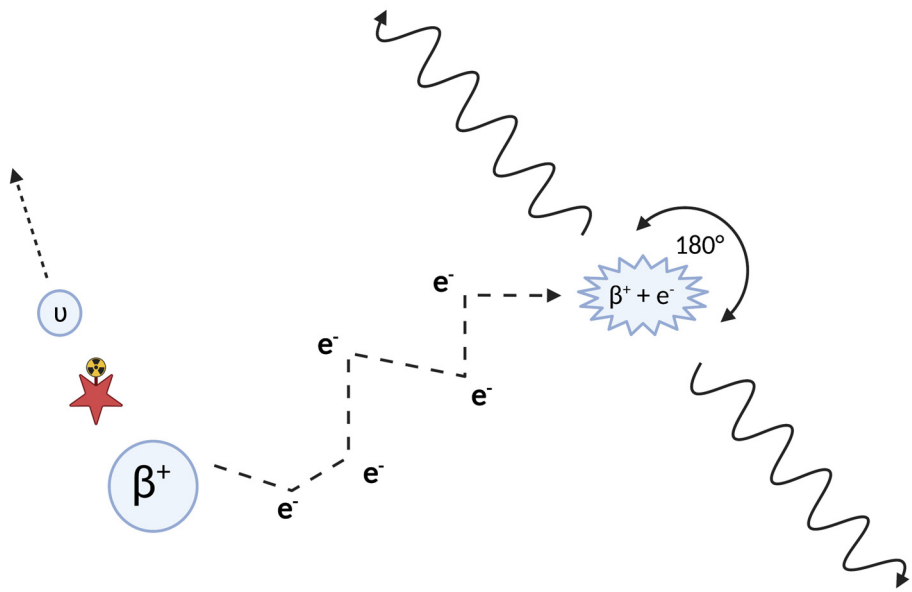

Figure 3.1 At the decay of the PET-tracer, a positron (β+) and neutrino (υ) is emitted. The positron loses its kinetic energy by interactions with electrons in the medium. When it as slowed down sufficiently it will annihillate with an electron. To conserve the energy of mass, two photons of 511 keV are emitted at approximatle 180˚. A small variance in the angle arise due to remaining kinetic energy, referred to as noncolinearity. Image inspired by (34). Created with BioRender.com.

Gamma and SPECT cameras depend on collimators to determine the direction of photons interacting in the detector volume. With a parallel hole collimator placed in front of the detector volume, only photons traveling perpendicularly, within a small

angular range, can pass through its holes; others will be attenuated in the collimator septa. The angular direction of the collimator holes is then the direction travelled of all detected photons. PET cameras, on the other hand, do not depend on collimators but detect coincident annihilation photons created when a positron emitted from the PET radiopharmaceutical annihilates with an electron at the end of its track. If the momentum of the electron-positron pair is zero at the time of annihilation, two 511 keV photons are emitted in opposite directions. The back-to-back emission of the two photons ensures that the momentum and energy is conserved in the annihilation process (Figure 3.1). Detecting both on the opposite side of the patient defines a line of response (LOR) through the body where the annihilation happened. This is sometimes referred to as electronic collimation.

For both PET and SPECT, scintillation crystals are still the most common detectors. Thallium-doped sodium iodine (NaI:Tl) crystals, the most commonly used SPECT detector, is however less suitable as a PET detector because of its poor absorption properties of 511 keV photons. Instead, higher density crystals with higher effective atomic numbers, such as cerium-doped lutetium oxyorthosilicate (LSO:Ce) and bismuth germanate (BGO) are necessary to increase the probability for full energy absorption of the 511 keV annihilation photons.

PET and SPECT data constitute of projections of the activity distribution inside the patient or animal, collected at different angles. To convert this into a 3D distribution of activity, image reconstruction must be performed. There are several mathematical approaches for tomographic reconstruction, however, a description of these is beyond the scope of this thesis (*34-36*).

3.2 PET camera design

Coincidence detection requires a PET system to have at least two detectors capable of measuring the timing of the interaction with high precision, enabling coincidence measurement of all the events taking place between the detector elements. The typical PET camera design consists of several detectors configured in a circle, facing the center of the ring (Figure 3.2 A). Multiple sets of detector rings forming a cylinder increase the axial field of view (FOV) and, consequently, the patient volume that can be imaged during the same time frame. Although PET cameras are more sensitive than SPECT cameras, far from all annihilation photons originating within the FOV will be detected in coincidence. In fact, most will not be detected at all. In many cases, only one of the photons from an annihilation pair will interact in a detector and cannot contribute

constructively to the image, as there is no information of the photon's trajectory from the point of the annihilation event.

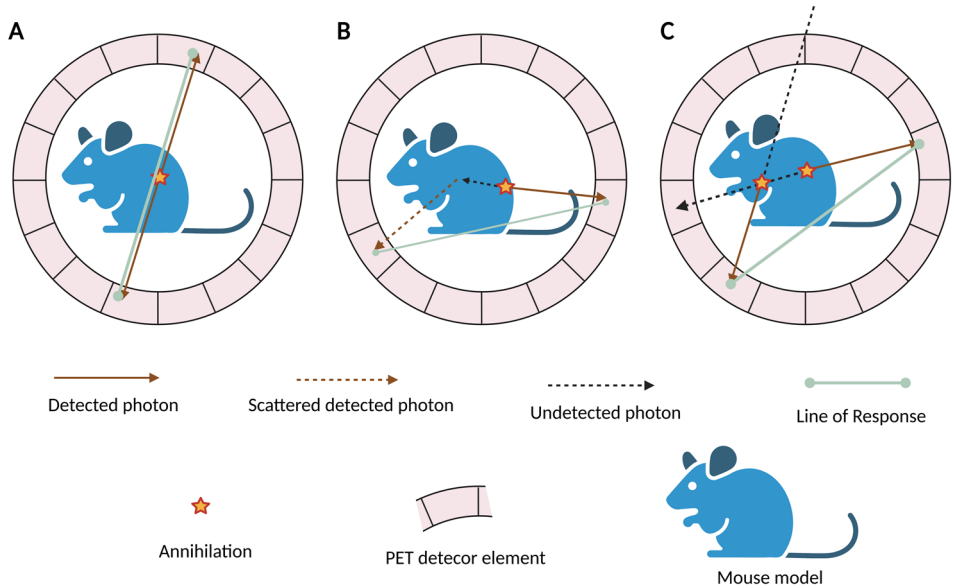

Figure 3.2 Schematic illustration of a standard PET camera. True coincidences (A) generate a LOR indicating the position of the annihilation event from where the coincident photons originated. Scattered events detected in coincidence (B) offset the LOR and reduce the spatial resolution. Random coincidences (C) appear when photons originating from different annihilation events are detected within the coincidence timing window and misinterpreted as a coincidence. Created with BioRender.com.

Under ideal conditions, a positron will have lost all of its energy at the end of its range and will annihilate with an electron. If the momentum of the electron-positron pair is zero, then two annihilation photons are emitted at a 180-degree angle to each other, in order to conserve energy and momentum. However, if the momentum of the electron-positron pair is non-zero, the emission of the annihilation photons will deviate from 180-degrees. This is commonly referred to photon non-collinearity [32] and will degrade the spatial resolution.

Photon pairs detected in opposite detectors form a LOR along which the annihilation event occurred. This case is referred to as a true coincidence (Figure 3.2 A). However, if one or both photons are scattered before interacting, the resulting LOR has no relationship to the position of the annihilation event (Figure 3.2 B). Also, two photons from two annihilation events can be misinterpreted as related if interacting in opposing detectors simultaneously, then referred to as a random coincidence (Figure 3.2 C). These carry no information of an annihilation event occurring along its LOR and will

only add noise and degrade the image contrast if not corrected for. The rate of random coincidences depends on the product of the single photon rates experienced by the two detectors in coincidence. Since the individual rates are proportional to the activity in the FOV, the random rate becomes proportional to the square of the activity (*34*).

The sum of all detected coincidences is often called prompt coincidences. To exclude random and scattered coincidences, a narrow timing window defines the maximum timing difference between events to be considered as coincidences, reducing the probability of random coincidences, and a narrow energy window excludes scattered photons that have lost enough energy. However, the detector's finite energy and timing resolutions will make perfect exclusion of unwanted coincidences impossible.

To perform quantitative PET, corrections must be made for several effects that reduce the proportional relationship between activity in the FOV and the detected number of coincidences. The number of detected random coincidences can be estimated for each LOR from the count rates experienced by the two detectors and subtracted from the prompt coincidences (*34*). Scattered coincidences add data to the prompt count rate and will reduce the image contrast and overestimate the activity. Dead time losses need correction to compensate for the loss of linearity between single rates in individual detectors and activity. Due to attenuation, activity at a larger depth in the body will be underestimated since their signal is reduced as photons are attenuated in the body. Corrections are necessary to even out this difference between shallow and deeply situated sources.

3.3 Preclinical PET

Preclinical PET systems mainly differ from clinical systems in size but are built with the same principles and components. In general, scanner operation, data acquisition, image reconstruction, and correction for attenuation and scatter are accomplished with the same or similar strategies as used for clinical systems (*34,35*).

Animal studies can be performed on clinical systems, but these often lack sufficient image quality. The smaller structures and volumes investigated in animals demand higher spatial resolution, and the lower injected activities require higher sensitivity. This has been a driving factor for the development of preclinical PET systems. As there is generally a tradeoff between spatial resolution and sensitivity, accomplishing both is a challenge, and a variety of more specialized preclinical PET systems have been designed for different applications (*34*). To receive an adequate spatial resolution, the detector element size must be reduced to match the dimension of the imaged structures

and are generally smaller than for clinical systems (*27*). Due to the non-collinearity of the annihilation emission, the loss of spatial resolution depends on the diameter of the detector ring, meaning smaller systems are less affected by the spatial resolution loss. Similarly, due to the comparatively small size of animal models compared to humans, less attenuation and scatter are caused along the trajectories of the annihilation photons.

Preclinical PET systems often have a larger axial coverage within the FOV, covering all or almost all from nose to tail, compared to when humans are imaged on clinical systems. This makes dynamical studies simpler and increases the sensitivity. However, clinical full body PET has become a growing research field and might find clinical applications in the future (*37*).

3.3.1 Imaging γ-H2AX as therapy response

The response to ionizing radiation in tumors can be seen in both early and late biological signals. As discussed earlier in chapter 2.2, cell death induced by ionizing radiation is primarily caused by DNA DSBs. The DDR chain causes a cascade of detectable signals, and some of these are manifested rapidly after damage induction. One of the most promising targets for radiation-induced damage investigated during the last decade is the previously mentioned γ-H2AX (*38*). It is a histone phosphorylated at the earliest steps of the cell DDR chain after induction of DSBs. γ-H2AX can be studied in biopsies, dissected tumors, xenografts, and tissues after irradiation to measure DNA DSB induction. Following the expression over time is a method for studying the DSB repair rate (*39-41*). Also, γ-H2AX have been studied in leukocytes in patients irradiated externally and with RPT (*42,43*).

With non-invasive molecular imaging such as PET and SPECT, in vivo diagnostics of the induced damage from a radiopharmaceutical could be detected and perhaps quantified. To utilize γ-H2AX for in vivo imaging, Cornelissen et al. created an anti-γ-H2AX antibody and labeled it with ^{111}In and (zirconium-89) ^{89}Zr for SPECT and PET imaging, respectively (*44,45*). Then, Knight et al. synthesized ^{89}Zr-anti-γ-H2AX-TAT and evaluated it in breast adenocarcinoma xenografts in mice irradiated with external beam irradiation to induce DNA damage (*46*). Since then, the same group has used this tracer to detect DNA DSBs during ^{225}Ac or ^{177}Lu pre-targeted radioimmunotherapy in mice bearing BxPC3 tumor xenografts (*47*).

O'Neill et al. imaged DNA damage with ^{111}In- anti- γ-H2AX -TAT in tumor-bearing mice while treated with 20 MBq ^{177}Lu-DOTATATE (*48*). Imaging of both radionuclides was accomplished with dual-isotope SPECT/CT. During the first 72 hours post-administration of ^{177}Lu-DOTATATE, the ^{111}In-anti-γ-H2AX-TAT signal

increased. This agreed with the increasing number of γ-H2AX-foci detected in cell lines irradiated with ^{177}Lu-DOTATATE in vitro.

The high sensitivity of quantitative PET would favor γ-H2AX-PET over γ-H2AX-SPECT. However, chelation strategies, the half-life of the radionuclides, biokinetics, etc., must be evaluated to find an optimal tracer. Similarly, the timing of imaging after the administration of the therapeutic radiopharmaceutical will greatly influence the result, as DNA DSB repair and cell death will alter the γ-H2AX tumor expression over time. O'Neill et al. performed longitudinal ^{111}In- anti- γ-H2AX -TAT imaging 1, 24, 48, and 72 h post ^{177}Lu-DOTATATE imaging (*48*) and saw ^{111}In uptake correlating to the ^{177}Lu-DOTATATE uptake in the tumor over all investigated time points. Similarly, Poty et al. imaged at several time points, up to 4 days after the administration of the therapeutic radiopharmaceutical and saw significantly higher uptake of ^{89}Zr-DFO-anti-γ-H2AX-TAT in ^{177}Lu-PRIT treated tumors compared to control at all time points (*47*).

Other tumor responses to radiation could be of interest to evaluate the therapeutic response to radiopharmaceutical therapy. For example, proliferation could be imaged with ^{18}F-FLT (*49*). Others include hypoxia (*50-52*), angiogenesis (*53*), and apoptosis (*54,55*). These may, however, be late responses manifesting when the therapeutic radiopharmaceutical has decayed sufficiently not to cause any significant disturbances to the quantification.

3.3.2 Limitations of intra-therapeutic PET imaging

Under normal circumstances, the PET tracer is the only source of photon emissions during a PET acquisition, and, naturally, those are the conditions PET systems are designed to handle. However, performing PET imaging during ongoing radiopharmaceutical therapy could be of great interest. For many radionuclides used therapeutically, this would mean a second source of photons causing interactions in the PET detectors.

^{177}Lu is successfully used in multiple radiopharmaceuticals for therapy, including ^{177}Lu-DOTATATE and ^{177}Lu-PSMA, and is often mentioned for its beneficial physical properties. Besides beta emission suitable for therapy, its decay is followed by the emission of a few photons, most prominently one of 113 keV (6.2 %) and one of 208 keV (10.4 %). These can be detected by SPECT imaging to investigate the uptake and are used for dosimetry applications (*56-59*).

If a PET acquisition is performed during an ongoing ^{177}Lu therapy, the high amounts of activity injected will contribute to a high fluence rate of photons unrelated to the

PET tracer. The photons emitted from ^{177}Lu will interact in the PET detectors, adding to the single photon event rate. Ideally, due to their low energy compared to the 511 keV annihilation photons, the energy window applied in most PET systems will exclude them, restricting them from contributing an increased random coincidence rate. However, two effects could still make them interfere with the coincidence detection of a PET tracer. These factors are pulse pile-up and dead-time.

The system electronics read out each pulse to analyze the pulse height. While the system is occupied with one pulse, it is "dead" to other incoming pulses that will then be lost (*13*). Dead-time characteristics are often schematically divided into "paralyzable" and "non-paralyzable." When paralyzed, new incoming pulses will extend the time the system remains dead. These systems will therefore have a peak count rate which will then fall for increasing activities. On the other hand, a non-paralyzed system will be able to detect a new event at the end of the dead-time window, unaware of any events appearing during the dead-time. Instead, these systems reach a count rate plateau so that increasing the photon fluence rate will no longer increase the count rate (*13,60*).

The PET detector's read-out rate is the time it takes to collect the signal and produce a read-out pulse. If two or more photons interact within a small enough time frame, the signals from these will be added and pile up and could be interpreted as a single pulse. The pulse will have the size of the summed energy deposited by the photons, which then might be large enough to pass through the coincidence energy window. The probability of pile-up will increase with the rate of interactions in the detector and, therefore, with increasing activity.

Contributions from a photon-emitting source other than the PET radiopharmaceutical could cause pile-ups, by adding false annihilation photons within the energy window. This could increase both detected random coincidences and dead-time losses as the system becomes busy analyzing the additional pulses generated by emission from the second source. This will result in a loss in detected true, un-scattered coincidence pairs.

Chapman et al. observed a similar effect when they attempted to combine SPECT and PET imaging on a preclinical PET system (*61*). Performing the imaging in sequence, beginning with SPECT followed directly by PET imaging, they noticed a PET signal loss at high ^{99m}Tc levels remaining from the SPECT image.

In paper 1, we investigated the effects of a second source of photon emissions on three preclinical PET systems (*62-64*). In this work, we used ^{99m}Tc as the second source of gamma emissions. With a gamma of 140.5 keV (89 %), it is the most frequently used radionuclide for gamma camera and SPECT imaging (*65*) and is not a candidate for therapeutic applications. The gamma emission of ^{99m}Tc is close to those of ^{177}Lu and

the shorter half-life allowed us to study the count rate effects continuously over a wide span of count rates within a reasonable time frame.

We allowed a source of ^{99m}Tc to decay in the FOV of the preclinical PET systems while continuously taking static images. Then, correcting for the decay, the images could be related to the ^{99m}Tc activity present during that time frame. To keep the true coincidence rate constant over the duration of the experiment, a ^{22}Na point source was used. With its long half-life of 2.6 years, the expected coincidence rate would not change significantly over the duration of these experiments. Detected changes were then assumed to be due to the second source of photon emissions. To verify the validity of using ^{99m}Tc as a gamma-emitting proxy, ^{177}Lu was used as the second source of gamma emission on one of the systems, alongside a ^{22}Na point source.

The spatial resolution, measured as the full width at half maximum (FWHM) over the ^{22}Na point source, and the prompt and random coincidence count rates are shown in Figure 3.3 for the preclinical PET systems Genisys4 (Sofie BioSciences) in A), Inveon (Siemens Medical Solutions) in B) and the NanoPET/CT (Mediso) in C). All systems showed a loss of spatial resolution at high enough ^{99m}Tc activities, but the activity necessary to cause this degradation differed greatly. Similarly, the prompt coincidence rates were affected on all systems. On two systems, the Genisys4 and the Inveon system, the prompt rate dropped at sufficient ^{99m}Tc activity, implying the second gamma source introduced dead-time losses in the detection of singles. On the NanoPET/CT, however, the prompt coincidence rate rose to a maximum with increasing ^{99m}Tc activity before dropping, implying pile-up caused an increased singles count rate that in turn generated random coincidences, adding to the prompt rate. On one system, the Genisys4, even low ^{99m}Tc activities, approximately 1-10 MBq, increased the random coincidence rate. For the other two, activities above 10 MBq ^{99m}Tc were necessary to observe an increase in random coincidences.

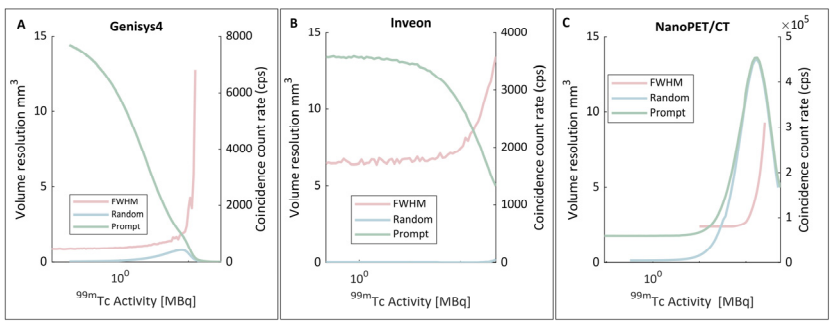

Figure 3.3 Evaluation of volume resolution (FWHM) and prompt and random coincidence count rate as a function of ^{99m}Tc activity on the Genisys4 system in (A), the Inveon system in (B), and the NanoPET/CT in (C). Adapted from figures in JNM (66).

The results showed the necessity to investigate the count rate characteristics of a preclinical PET system before attempting intra-therapeutic PET imaging. It can therefore not be assumed that the energy window will reject the extra photon interactions without effects on the spatial resolution or quantitative abilities. Ignoring these effects could generate inaccurate data and compromise the results of the intended study.

A plausible concern arises when performing longitudinal studies, imaging at multiple time points after administrating the therapeutic radiopharmaceutical. The initial time point might be highly perturbed due to the presence of the therapeutic radiopharmaceutical, leading to erroneous activity quantification. At later time points, the therapeutic activity will have decayed, and the perturbation effects may have changed, making activity quantification at different times uncertain.

Our method used ^{99m}Tc instead of ^{177}Lu to investigate preclinical PET system's limitation to perform intra-therapeutic imaging. Starting with a high ^{99m}Tc activity and allowing it to decay, high-to-low interaction rates can be measured over a much shorter time without removing the sources, thanks to the shorter half-life of ^{99m}Tc. However, the differing yields and slightly different linear attenuation coefficients of the ^{99m}Tc and ^{177}Lu photon emissions must be considered to estimate the necessary ^{177}Lu activity generating a similar perturbation of the system. Taking these factors into account, ^{177}Lu will generate approximately 1/5 of the interactions caused by ^{99m}Tc per unit activity, meaning a ratio of 5 can be used to convert the activity between the two radionuclides.

Under normal imaging conditions with only the PET tracer, dead-time corrections are commonly applied to compensate for count losses. Since a PET camera typically registers both the single photon rate and the coincidence rate, dead-time in both circuits must be considered. This is sometimes done by estimating the losses based on the singles rates. A different method estimates dead-time from the triple coincidence rate, when a true coincidence pair is detected simultaneously as a third annihilation photon or three unrelated annihilation photons are detected within the coincidence timing window (*60*). However, since the high photon fluence rate will not be due to the PET tracer during intra-therapeutic imaging, these methods will not correctly estimate losses from the PET tracer but misinterpret detected photons from ^{177}Lu as single annihilation photons. The approximate relationship between singles and coincidences is lost, and the compensating methods could potentially introduce additional errors.

4 Monte Carlo simulations in nuclear medicine

Monte Carlo (MC) simulations are used to study a wide range of problems by simulating stochastic processes, such as radiation interacting with matter, where the likelihood of a given interaction can be described by a probability density function (PDF). Therefore, MC simulations have many applications in radiation physics and medical physics. For example, the simulation of medical imaging systems enables the estimation of scattered photons and their effect on image quality. Similarly, the energy imparted to a volume can be simulated. This allows the estimation of the absorbed dose from a radiating source, which is valuable for radiotherapy and RPT applications.

The simulations are used to calculate such parameters as photon and particle transport, energy deposited, deflection angles, etc., for multiple events. As the number of simulated events (often called histories) increases, the resulting distributions converge toward the "true" distribution, and the statistical error decreases. This is particularly useful for problems that can't be solved analytically but only be estimated through experiments or simulations. In that sense, simulations are a model of an experiment run multiple times to evaluate the solution. It can estimate values unattainable to us by measurement, such as effects in vivo, where no detector can be placed. These estimates' accuracy will depend on the models provided, simulation geometry, materials and source descriptions, and PDFs of the physical interactions. While simplifications, often called variance reduction techniques, can be well-motivated to speed up the simulations, it is crucial not to misrepresent or exclude a parameter that significantly impacts the results. A standard method to reduce simulation time is by applying energy limits, below which histories are no longer tracked.

4.1 Monte Carlo simulations for nuclear medicine in GATE

The GATE (*67,68*) (**G**eant4 **A**pplication for **T**omographic **E**mission) program is an MC simulation environment originally aimed at tomographic imaging applications, but it has found multiple applications in medical physics and nuclear medicine beyond that. It uses Geant4 (*69,70*), developed at CERN, as its physics engine and allows the user to describe the simulation setup in macro files with simple commands. The user does not need to code directly in C++, as otherwise necessary to interact with Geant4.

MC simulations are based on sampling random numbers from a pseudo-random algorithm (*71*). An initial number, often called a seed, calculates a series of random numbers. This exact sequence of numbers is reproduced if the same seed is used again. There is a potential risk that these algorithms repeat themselves if used to generate an extensive series of numbers. Therefore, they are considered pseudo-random since it might be unclear when this limit is reached. In GATE, three different random number generators are available. For the simulation work in this thesis, the default algorithm Mersenne Twister was used for all simulations (*72*). The random number generator is used to sample the PDFs of the implemented physics models. Depending on the nature of the process described by the PDF, the sampling can be performed in multiple ways. For example, Geant4, and thereby also simulations run by GATE, uses a combination of the composition method and the rejection method to perform sampling of PDFs (*73*).

For nuclear medicine imaging applications, it is often sufficient to simulate the interaction of photons, such as gammas. For example, the purpose might be estimating the ratio of photons scattering within a volume, such as a patient's body, before exiting it. Secondary electrons released by photon interactions, such as an electron released during Compton scattering, are often unnecessary to simulate directly and can be assumed to be absorbed locally, as they will not affect the signal detected in a simulated imaging system. However, for radiopharmaceutical therapy applications, it is necessary to simulate the interactions of charged particles as these are directly ionizing and depositing energy to matter. Since photon and charged particle interactions differ fundamentally, they must be handled differently.

As explained in a previous chapter, the linear attenuation coefficients describe the probabilities for photons interacting with matter. These are available as tabulated values from databases (*74*) for different photon energies, elements, and materials. For composite materials, the total attenuation coefficients can be calculated. Photon interactions will lead to photon tracks ending with absorption or being scattered in new

directions. Models of these interactions are used to sample new energies and directions at interaction points. Commonly, in a simulation of a photon, the path length before an interaction is calculated based on the mass attenuation coefficient. At the resulting coordinates, a new energy and direction are calculated. If the photon is fully absorbed, the history ends. Otherwise, a new path is calculated from the new photon energy and direction. This is repeated until the photon is either fully absorbed or leaves the volume of the simulation, or if energy thresholds are implemented, the photon has lost enough energy to fall under this threshold. It is then considered fully absorbed at this point.

Charged particles lose their energy to the surrounding material through multiple interactions. Over the range of a single electron, millions of interactions may occur, predominately inelastic scatter, making a detailed simulation of every step very time-consuming or practically impossible. The standard solution to this is calculating a condensed history of charged particles. As each interaction only changes the energy and direction by a minimal amount, the tracks are summed in larger steps. These are calculated with multiple scatter models (*74,75*). GATE and Geant4 provide several models for this purpose.

GATE prompts the user to choose a physics list from the Geant4 library. These are predefined packages of physical models. Depending on the nature of the simulation, such as the energy range of the primary emissions and the size of the volumes in the simulation world, these packages have been tailored to meet many different needs. Other models can be added manually if a package is not sufficiently specific to the needs of the simulation. In the simulations run in the work of this thesis, the physics list *emstandard_opt3* has been applied to all simulations (*76*). This package contains models of all relevant electromagnetic interactions necessary for both photons and charged particles for energies relevant to the projects of this thesis.

4.2 Building GATE Monte Carlo simulations

When building and interacting with a simulation in GATE, a set of commands are used to describe the nature of the simulation. These are written in macro files that are read by GATE and used to set up the simulation in the Geant4 engine. This simple form of scripting is meant to make MC simulations for medical physics more accessible to those who have not yet mastered C++ programming. Also, GATE contributes a toolbox of functions explicitly aimed at medical applications. Some of these, implemented in the projects of this thesis, are reviewed below. Note that in the following description of working with GATE, all emissions, including photons, are described as particles, which is consistent with the language used in the GATE documentation (*72*).

4.2.1 The GATE world, geometry, and materials

In the initial step, the user defines the simulation world and its volumes. Basic geometrical shapes, such as boxes, cylinders, and spheres, can be generated, and more complex ones can be built from combinations of these. Also, voxel or mesh volumes from external data, such as a CT scan, can be loaded into the world description.

In project 2, the water-filled volume of a syringe was modeled as a cylinder. To generate this in GATE, the simple commands in Figure 4.1 were used:

```
/gate/world/daughters/name                    Syringe
/gate/world/daughters/insert                  cylinder
/gate/Syringe/setMaterial                     Water
/gate/Syringe/geometry/setRmax                1. cm
/gate/Syringe/geometry/setHeight              5. cm
```

Figure 4.1 GATE script to generate a water-filled volume.

Volumes are daughters of the world, meaning they inherit properties of the world if not otherwise stated. Similarly, volumes can have their own daughters, such as a subunit of a volume. This is commonly used to define detector elements in a detector panel but can have other applications.

In paper 3, z-stack images of DAPI-stained PC3 cell nuclei imaged with confocal microscopy were segmented as 3D mesh volumes and saved in STL files. In GATE, the mesh volumes were placed on a surface under an alpha-emitting source to simulate cells being irradiated in vitro by an ^{241}Am source. To read the mesh volumes into the GATE world, the volume type was declared "tessellated," and the path to the file was defined, as in Figure 4.2. The cells are daughters of the volume "CellLayer" in the simulation.

```
/gate/CellLayer/daughters/name                stlcell
/gate/CellLayer/daughters/insert              tessellated
/gate/stlcell/geometry/setPathToSTLFile       data/STLPhantom/Vol.stl
```

Figure 4.2 GATE script to import a mesh volume into the GATE simulation world.

An appendix to the main macro file defines elements and materials. They can then be applied to volumes of the simulation world, thereby defining the nuclear properties needed to calculate the simulated physical interactions. Elements are defined by their atomic number and molar mass and can be used to scale the linear attenuation coefficients. Composite materials can be defined by stating the abundance of elements included and the material's density.

Surrounding the syringe in project 2, a hollow cylinder was placed to simulate a Rose metal shield. Rose metal is an alloy of bismuth (Bi), lead (Pb), and tin (Sn). To declare this as a new material, the lines in Figure 4.3 were added to the GATE materials database:

```
Rose:   d=9.85 g/cm3; n=3; state=Solid
        +el: name=Bismuth    ; f=0.500
        +el: name=Lead       ; f=0.280
        +el: name=Tin        ; f=0.220
```

Figure 4.3 Defining the properties of Rose metal by declaring the fraction of the elements making up the new material, and the density.

The density (d), number of included elements (n), and physical state were declared. Each element and its fraction in the new material was stated. Then, when generating the shield in the GATE macro, the new material Rose can be implemented as in Figure 4.4.

```
/gate/world/daughters/name                      shield
/gate/world/daughters/insert                    cylinder
/gate/shield/setMaterial                        Rose
/gate/shield/geometry/setRmax                   3 cm
/gate/shield/geometry/setRmin                   1.1 cm
/gate/shield/geometry/setHeight                 50. mm
```

Figure 4.4 Gate script defining the shield and stating the new material "Rose."

When GATE is used for simulating a tomographic imaging system, the type of system must be declared. This creates a structure for volumes defined to be intricate parts of the system. It enables GATE to output a list of interactions in individual detector elements. These hits can then be used in a *digitizer*, a model of the signal processing that is used to transform the hits into digital pulses. It can include energy and timing resolution, thresholds, and system dead-time effects. After processing, hits that pass through the digitizer chain are called singles. For PET cameras, these can then be fed into a coincidence digitizer step to find pairs of singles that are accepted as coincidences. This was implemented in paper 2 (see section 4.2.4).

4.2.2 GATE sources

Sources can be generated in multiple ways in GATE, enabling both simulations of beam geometries, radionuclides in a source volume, or more artificial geometries such as point sources. Emissions can be isotropic or radially limited. In addition, multiple sources can be defined in the same simulation.

General purpose sources (GPS) are stated by selecting from a list of particles, such as electrons, positrons, and photons. The energy, shape, angular distribution, placement, and, if applicable, movement of the source can be specified. Sources can be monoenergetic or follow a given emission spectra. Some special sources for standard, specific simulations are provided, such as for the simulation of fluorine-18 (^{18}F). For example, when simulating a positron source, GATE can implement the positron energy spectrum of ^{18}F. Or, if the positron can be neglected, the commando "back-to-back" can instead generate two 511 keV photons at 180 degrees from the source point. This is a simplified and often faster approach if the path length of the positron and the angular distribution of the annihilation photons can be ignored.

Ion sources, where a specific ion is simulated by stating the atomic number (Z), the atomic weight (A), ionic charge (Q), and excitation energy (E), give a realistic model of the radioactive decay and emission of the stated radionuclide. It uses emission data from the ENSDF database (*73*). The simulations, therefore, become very realistic but often very time-consuming. On the other hand, excluding emissions at a low yield or simulating a monoenergetic emission of the mean emission energy is a variance reduction technique that can be well motivated for some simulations that make them less computationally heavy.

```
########### HistogramSpectrumLu177.txt ##########
   2    0
   0         0.00547734
   0.0005    0.00550233
   0.0010    0.00551093
   0.0015    0.00550312
   0.0020    0.00549469
   0.0025    0.00548678
   ..........................................
   ..........................................
   ..........................................
```

Figure 4.5 Stating a histogram spectrum of beta energies for ^{177}Lu.

A third way, a compromise of a simple monoenergetic source and an unnecessarily complex ion source, is stating an energy spectrum in a separate file, called a *User Spectra*, and applying it to a GPS. These can be discrete spectra, histogram spectra, or linear interpolated spectra. In papers 3 and 4, sources were defined as discrete and histogram spectra. In paper 4, the alpha particle emissions of ^{225}Ac and its daughters in the decay chain were simulated by stating the alpha particle energies and relative intensity in a discrete spectrum file and connecting this to the source volumes of the simulation geometry. When instead simulating the beta emission of ^{177}Lu in the same paper, a histogram spectrum file was set up with the energy binned in 0.005 MeV wide bins in

the first column and the relative intensity in the second column, as in the example in Figure 4.5.

4.2.3 GATE Actors

GATE has a set of functions aimed at simplifying simulations for medical physics problems. These are called *Actors*, as they are tools that interact with the simulation by measuring some parameter or changing a simulation setting when specific criteria are filled. Actors can have a shape and volume, such as the geometrical volumes in the simulations. Often, it is likely that the Actor has the same shape as a given volume, and the actor can therefore be attached to a declared volume. If not otherwise stated, it will have the same position and shape as the volume it is linked to. Some actors can generate a 2D or 3D matrix output, such as an absorbed dose image. The user sets the spatial resolution of the output image. If the Actor is attached to a volume not shaped like a box, the output matrix will be the bounding box of that volume. Actors can be filtered to only act on or record data of specified types of particles or energy intervals of particles.

The *Dose Actor* measures the energy deposited in a volume and can calculate the absorbed dose from the declared material and the density of that volume. As utilized in paper 3, simulating alpha particles irradiating cell nuclei, the Dose Actor can count the number of hits of a specific particle type. In paper 4, the Dose Actor took the same shape and resolution as the source volumes declared in the simulation.

The *Phase-Space Actor* can record multiple data about particles entering the actor, such as kinetic energy, position, and direction along the three axes. As utilized in paper 3, the result of a Phase-Space Actor can be used as a source in another simulation. The output file is then used as input to declare the energy and angular distribution of emissions from the new source. This can be particularly useful when only a small portion of the source emissions reach the target volume of interest. Instead of simulating the entire transport of all particles until enough particles have reached the target volume to achieve a low enough statistical uncertainty, the transport to the initial step is simulated to a Phase-Space Actor closer to the target volume, there measuring the fluence properties and using this data when generating new particles in the second step of the simulation.

The *Energy Spectrum Actor* stores the energy, energy deposition, and LET of particles entering the Actor in histograms. The user specifies the binning and range to consider for these histograms. They are used in paper 3.

4.2.4 Intra-therapeutic imaging simulations

As the results of paper 1 showed, preclinical PET imaging during an ongoing ^{177}Lu therapy could significantly influence image quality and the system's quantitative abilities. Therefore, as a follow-up in paper 2, the reduction of image quality and the quantitative breakdown was investigated on the G8 preclinical PET system, an upgraded version of the predecessor Genisys4. This time, a solution to the problem was suggested.

Since the gamma emissions from ^{177}Lu and the resulting 511 keV annihilation photons from PET radionuclides differ in energy, so does the attenuation coefficient, especially in heavy materials, such as metals. The attenuating effect is greater on low-energy photons, while the high-energy annihilation photons will more often pass through a metal filter without interacting. Effectively, the filter will mainly attenuate photons emitted from ^{177}Lu, while the annihilation photons have a higher probability of passing unaffected.

Lead is commonly used to shield radioactive sources. Containers for radionuclides and radiation protection shields are commonly made of lead. It is often easier to mold when used in alloys and less toxic. Rose metal is an alloy of lead, bismuth, and tin, useful when making custom-made radiation protection shields for clinics and laboratories. To investigate the usefulness of shielding in intra-therapeutic preclinical PET imaging, we molded Rose metal shields (Figure 4.6) as hollow cylinders, large enough to fit a mouse, and small containers for radioactivity, such as syringes, inside.

Figure 4.6 Rose metal shield for intratherapeutic preclinical PET imaging.

Shielding in PET cameras is not new but has been used for different purposes. For example, both graded absorbers and lead filters have been implemented in PET systems

to reduce the number of photons scattered in the patient reaching the detectors (*77,78*). Also, in early attempts to combine PET and CT to perform simultaneous imaging, Goertzen et al. shielded the PET detectors from x-rays with lead shields (*64*).

The spatial resolution, measured as the FWHM of a line profile drawn over a ^{22}Na point source, a long-lived positron-emitter generally used for system quality control and calibrations, deteriorated in the presence of increasing ^{177}Lu activity (Figure 4.7 A). The image counts detected in a volume of interest inside a cylinder with 790 kBq ^{18}F imaged with increasing ^{177}Lu activity initially increased but then fell off for increasing ^{177}Lu activity (Figure 4.7 B). This loss of quantitative ability compromises longitudinal intra-therapeutic studies since the ^{177}Lu activity in a treated animal will change over time due to radioactive decay and excretion. Rose metal shields (2-4 mm) restored the spatial resolution, with no significant difference between the thicknesses investigated, and made the image count rate independent of the ^{177}Lu activity present. Similarly, all shields generated a constant image count rate independent of ^{177}Lu activity. However, the system-specific activity calibration factor would have to be recalibrated for the shield thickness used to avoid underestimating the activity. When investigating a VOI over the ^{22}Na source, the coincidence count rate increased somewhat for the 2 mm shield, and the image count rates dropped as the ^{177}Lu increased, implying that 2 mm Rose metal might be a little too thin to completely eliminate the effects of the ^{177}Lu source. No such implications were seen for 3 or 4-mm rose metal shields.

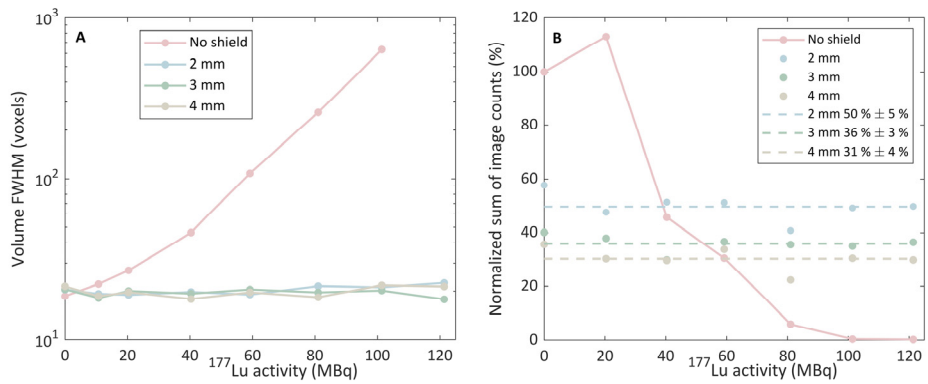

Figure 4.7 Image volume resolution evaluated as the FWHM of a ^{22}Na points source, (A), and the normalized amount of image counts in a VOI centered in a cylindrical container holding 790 kBq ^{18}F (B), with increasing thickness of Rose metal shielding (0 - 4 mm). Modified from image published in JMN (*79*).

When tested in vivo, a real proof-of-concept example was generated. A tumor-bearing mouse injected with 790 kBq ^{18}F-FDG was imaged, first by itself (Figure 4.8 A), with 120 MBq ^{177}Lu in a small container on its back (Figure 4.8 B), and finally with a 4 mm

Rose metal shield surrounding both activity sources (Figure 4.8 C). As clearly shown, all image information is lost due to the presence of the high ^{177}Lu activity (Figure 4.8 B) but is restored when using the shield (Figure 4.8 C). Furthermore, the shielded image was nosier since the acquisition time was kept the same for all images, allowing fewer true coincidences to occur in the shielded case. Therefore, prolonged acquisition time or increased ^{18}F-FDG activity could have compensated for some signal loss.

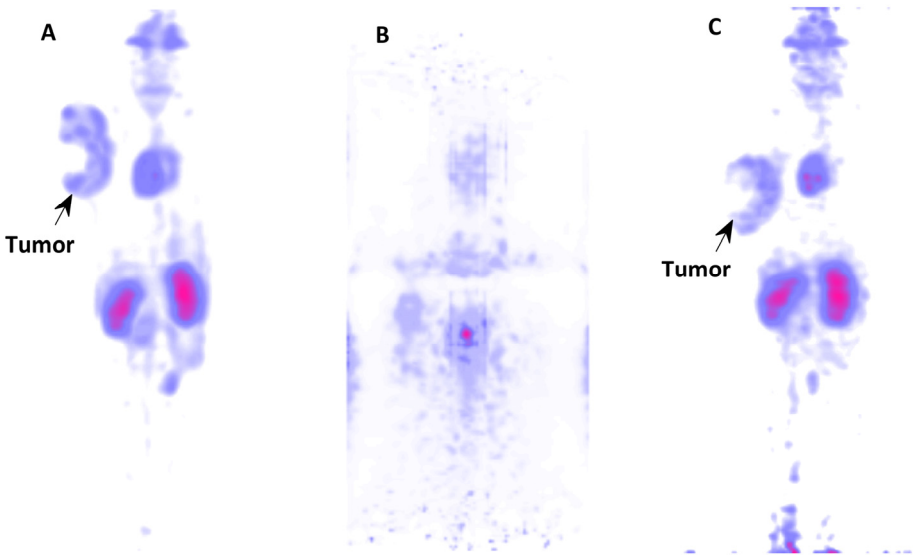

Figure 4.8 One C57BL/6 mouse bearing an RMI-PGLS-based subcutaneous tumor in the shoulder injected with 790 kBq ^{18}F-FDG imaged on the G8 preclinical PET system one hour after injection in (A). Next, the mouse was imaged again in the presence of 120 MBq ^{177}Lu in a container taped to its back in (B). Finally, a 4 mm Rose metal shield was inserted around the mouse and the ^{177}Lu-filled container and imaged one final time in (C). Modified from image published in JNM (*79*).

Monte Carlo simulations in GATE were performed to investigate the underlying reasons for the signal loss. A GATE macro describing a model of the preclinical PET system Genisys4 was kindly made available to us by Zheng Gu at the Crump Institute, UCLA. In addition, the model of a water-filled syringe and a Rose metal shield was added to the same simulation geometry.

A digitizer model was implemented to investigate the effect of a ^{177}Lu source present simultaneously with a ^{18}F source in the water volume on the singles and coincidence count rates. In a simulation, a volume declared as a detector outputs hits. These are a list of the physical interactions in the volume and are not the output signal of an actual detector. To simulate the processing leading to a digitized output, a chain of events is described in the digitizer macro. The user can access hits at different *depths* of the

detector. The first depth is the whole detector, independent of any specific sub-volume the interaction took place in. A simulated PET detector is commonly subdivided into sectors, referred to as the second depth. In addition, the sectors are often divided into smaller volumes, representing the individual crystal elements, referred to as the third depth of the detector.

The steps of the digitizer model are summarized in Figure 4.9. Also, the macro script of the digitizer is presented in Figure 4.10. First, our model generated a category of digitized output, *Singles*, where all hits in a detector block, in any of its crystal elements (Depth 1), were added to the singles. If a single particle generates multiple hits within a detector volume, the *adder* of the digitizer sums these up as a pulse. The *readout* depth defines at which level the electronics read the pulses.

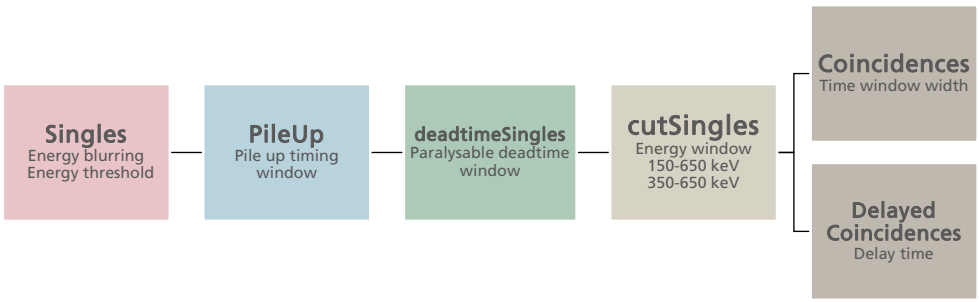

Figure 4.9 Digitizer flow chart. The steps included in the digitizer model, processing the detector output to generate the simulated PET camera coincidence count rate.

The singles remaining after all digitizing steps, the ones in *cutSingles*, were fed into two parallel coincidence steps—the first, detecting coincidences within the declared timing window. If multiple possible coincidence couples were detected, the *takeWinnerofGoods*-command prompts GATE to only consider the two with the highest energies as a coincidence. The second is used to estimate the delayed coincidences, often calculated by PET systems as an estimate of the random coincidences. Here, the coincidence window has a large enough delay that coincidences detected are certain to not originate from the same positron annihilation event.

```
############ DIGITIZER ##############
#ADDER
/gate/digitizer/Singles/insert                                adder

#READOUT
/gate/digitizer/Singles/insert                                readout
/gate/digitizer/Singles/readout/setDepth                      1

#BLURRING
/gate/digitizer/Singles/insert                                blurring
/gate/digitizer/Singles/blurring/setResolution                0.26
/gate/digitizer/Singles/blurring/setEnergyOfReference         511. keV

# LOW ENERGY CUT
/gate/digitizer/Singles/insert                                thresholder
/gate/digitizer/Singles/thresholder/setThreshold              {threshold} keV

### Pile-Up
/gate/digitizer/name                                          PileUp
/gate/digitizer/insert                                        singleChain
/gate/digitizer/PileUp/setInputName                           Singles

# PILE UP
/gate/digitizer/PileUp/insert                                 pileup
/gate/digitizer/PileUp/pileup/setDepth                        3
/gate/digitizer/PileUp/pileup/setPileup                       {pileup} ns

### NEW   BRANCH deadtimeSingles
/gate/digitizer/name                                          deadtimeSingles
/gate/digitizer/insert                                        singleChain
/gate/digitizer/deadtimeSingles/setInputName                  PileUp

# DEAD TIME / BLOCK
/gate/digitizer/deadtimeSingles/insert                        deadtime
/gate/digitizer/deadtimeSingles/deadtime/setDeadTime          {deadtime} ns
/gate/digitizer/deadtimeSingles/deadtime/setMode              paralysable
/gate/digitizer/deadtimeSingles/deadtime/chooseDTVolume       rsector

### NEW BRANCH cutSingles
/gate/digitizer/name                                          cutSingles
/gate/digitizer/insert                                        singleChain
/gate/digitizer/cutSingles/setInputName                       deadtimeSingles

# ENERGY THRESHOLD
/gate/digitizer/cutSingles/name                                  highThresh
/gate/digitizer/cutSingles/insert                                thresholder
/gate/digitizer/cutSingles/highThresh/setThreshold               [LD] keV
/gate/digitizer/cutSingles/insert                                upholder
/gate/digitizer/cutSingles/upholder/setUphold                    {HD} keV

### COINCIDENCES
/gate/digitizer/Coincidences/setInputName                        cutSingles
/gate/digitizer/Coincidences/setOffset                           0. ns
/gate/digitizer/Coincidences/setWindow                           {window} ns
/gate/digitizer/Coincidences/MultiplesPolicy                     takeWinnerOfGoods

# DELAYED COINCIDENCES
/gate/digitizer/name                                             delay
/gate/digitizer/insert                                           coincidenceSorter
/gate/digitizer/delay/setInputName                               cutSingles
/gate/digitizer/delay/setWindow                                  {window} ns
/gate/digitizer/delay/setOffset                                  {delay} ns
```

Figure 4.10 Digitizer Gate script.

To simulate the energy resolution of the BGO scintillators, an energy blurring of 26 % was implemented. A low energy threshold was used to exclude pulses at the low end of the energy spectrum. Next, a new category was generated, *PileUp*, to simulate the timing resolution of the detector. Pile-up of events happening within a narrow time window was calculated by us at the individual crystals level (depth 3) for singles appearing within the timing window. The *PileUp* singles were fed to a dead-time step, where singles happening within the dead-time window of a previous single were lost in the *deadtimeSingles* category. The system dead-time response was assumed to be paralyzable. Next, to simulate the energy window commonly used in PET systems to identify unscattered annihilation photons, those falling outside the energy window were removed from *cutSingles*.

The digitizer model was initially optimized by modifying the pile-up timing, dead time, and low-energy threshold. Varying these will shift the position of the peak count rate and the width and tail of the count rate curves. Measured singles and coincidence count rates from a decaying ^{18}F source measured on the Genisys4 system were compared to the digitizer output *cutSingles* and prompt coincidences of the digitizer model. The best agreement was found for a pile-up window of 200 ns, a deadtime window of 1550 ns, and a low energy threshold of 10 keV.

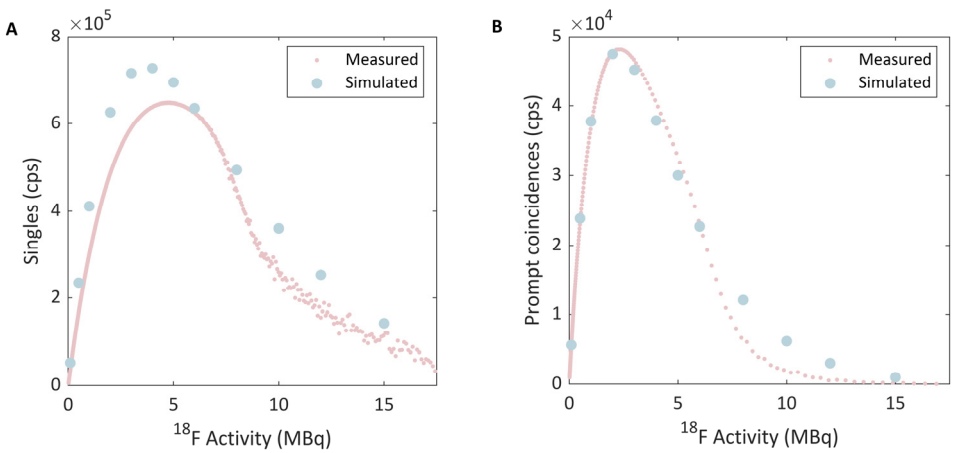

Figure 4.11 Digitizer optimization results. Simulated singles count rate (A) and prompt coincidence count rate (B) compared to measured count rates on the Genisys4 system. Modified from figure published in JNM (*79*).

As seen in Figure 4.11 B), the model recreated the detected prompt coincidence rate to a high degree, however, at high activity levels the rate was somewhat overestimated. The simulated singles rate showed lower degree of agreement with measured results,

showing a consistent overestimation of the rate, and not fully reproducing the shape of the count rate response. The simulated peak rate activity was also observed to be lower compared to measurements (Figure 4.11 A). The overestimation is not unexpected, as the model only consists of a few signal-modifying steps. The actual signal processing chain is most likely more complex and able to sort out more unwanted events, thereby generating a lower rate. Nevertheless, the good agreement with the coincidence rate was a convincing result that the model was sufficient for the purposes of this paper.

```
##F-18 point source
/gate/source/addSource                                  f18
/gate/source/f18/setActivity                            100000 becquerel
/gate/source/f18/gps/particle                           e+
/gate/source/f18/setForcedUnstableFlag                  true
/gate/source/f18/gps/energytype                         Fluor18
/gate/source/f18/setForcedHalfLife                      6586 s
/gate/source/f18/gps/type                               Volume
/gate/source/f18/gps/shape                              Cylinder
/gate/source/f18/gps/radius                             0.5 mm
/gate/source/f18/gps/halfz                              0.5 mm
/gate/source/f18/gps/angtype                            iso
/gate/source/f18/gps/centre                             0. 0. 0. cm
```

Figure 4.12 Gate script to generate a ^{18}F source inside a cylinder

The digitizer model was therefore included in a simulation of two sources decaying simultaneously in the FOV of the Genisys4 camera. To simulate the photons interacting in the detector volumes, a small cylindrical ^{18}F source was generated as a GPS at the center of the PET camera FOV. The ^{18}F positron energy distribution was employed by stating the energy type “Fluor18”, as in Figure 4.12.

```
##Lu-177 source in cylinder
/gate/source/addSource                                  lu177
/gate/source/lu177/setActivity                          {Act} becquerel
/gate/source/lu177/gps/particle                         ion
/gate/source/lu177/gps/ion                              71 177 0 0
/gate/source/lu177/setForcedUnstableFlag                true
/gate/source/lu177/useDefaultHalfLife
/gate/source/lu177/gps/type                             Volume
/gate/source/lu177/gps/shape                            Cylinder
/gate/source/lu177/gps/radius                           1.0 cm
/gate/source/lu177/gps/halfz                            2.5 cm
/gate/source/lu177/gps/angtype                          iso
/gate/source/lu177/gps/centre                           0. 0. 0. cm
```

Figure 4.13 Gate script to generate a ^{177}Lu general-purpose source attached to a cylinder volume.

In contrast, the ^{177}Lu source was generated as an ion source, shaped as a cylinder the same size as the water-filled volume of the syringe. The activity of the ^{18}F source was simulated as 100 kBq. The simulation was rerun for varying activity of ^{177}Lu. Using a placeholder in curly brackets, the activity of ^{177}Lu could be declared at the start of the simulation run without editing the macro file, as exemplified in Figure 4.13.

Investigating the origin of the photon interactions in the detector volumes revealed a high abundance of interactions caused by the emission from the ^{177}Lu source, as seen in the energy spectrum of simulated hits in the detectors in Figure 4.14 A. Even if these can be excluded by a narrow energy window in the digitizer chain, they are still occupying the system in the previous steps, paralyzing it by prolonging the dead-time, or they can contribute to pile-up as the probability will increase with increased count rates. In Figure B), using a 4 mm Rose metal shield reduced the total number of hits per second and the portion of hits originating from ^{177}Lu emissions. Using the shield, only 9.2 % of the hits detected originating from ^{177}Lu emissions without the shield now interacted in the detectors, compared to 57.9 % for emissions from ^{18}F.

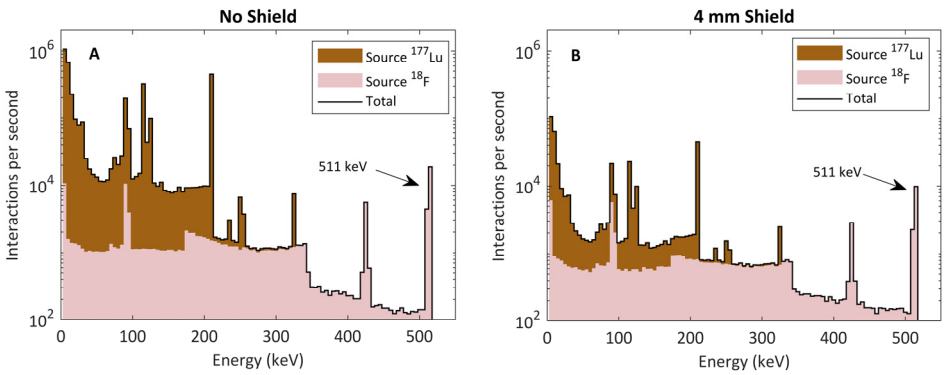

Figure 4.14 Energy distribution of simulated photons interacting in the detector volumes originating from the 10 MBq ^{177}Lu or the 100 kBq ^{18}F source (A). The energy distribution of interacting photons when a 4 mm rose metal shield was simulated surrounding the source (B). Modified from image published in JNM (*79*).

The output of the digitizer model for increasing ^{177}Lu activity is seen in Figure 4.15. The initial number of hits in the detector volumes are added up as detected pulses, called singles. Simulating pile-up somewhat reduced the count rate, especially at high activity levels, but the largest impact was the dead-time losses for the investigated activities. Applying the energy window excluded all events outside of the window limits.

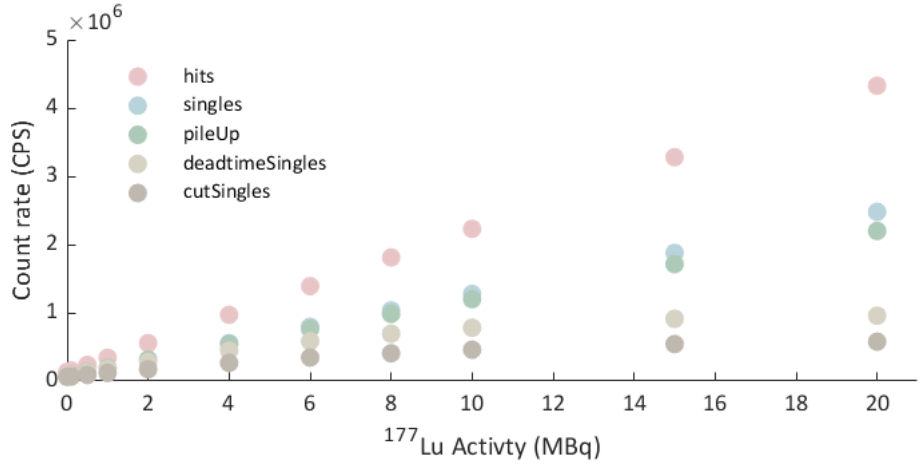

Figure 4.15 Resulting number of hits count rate in the simulated detectors volumes and the resulting singles, pileup, deadtimeSingles, and cutSingles count rate from the digitizer model, simulating 100 kBq of ^{18}F and increasing levels of ^{177}Lu activity.

The resulting prompt coincidences simulated for a 100 kBq ^{18} F source and increasing activity of ^{177}Lu are seen in Figure 4.16. Similar to measured rates on the G8 camera, the coincidence count rate decreased continuously with increasing ^{177}Lu activity. Still, a constant count rate independent of the ^{177}Lu activity could be achieved with a Rose metal shield.

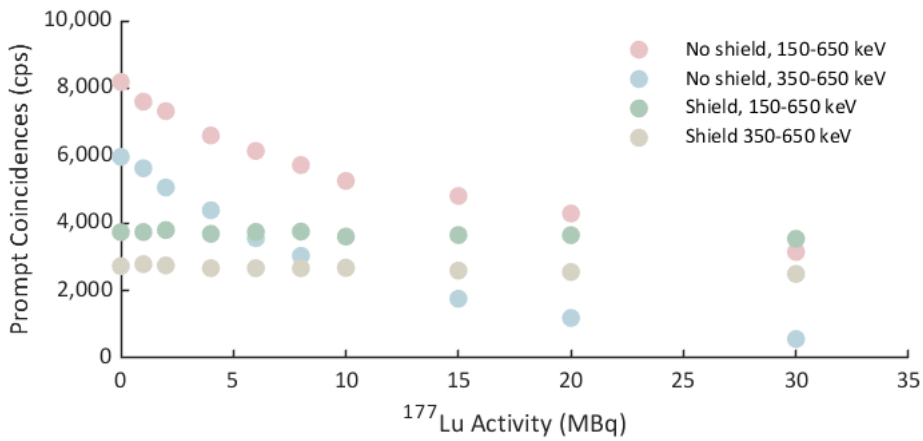

Figure 4.16 Simulated prompt Coincidence count rate from 100 kBq ^{18}F and increasing ^{177}Lu activity for a wide energy window (150-650 keV) and a narrow energy window (350-650 keV) with and without a 3 mm rose metal shield surrounding the sources. Modified from image published in JMN (*79*).

5 Dosimetry

Dosimetry of ionizing radiation is performed under the assumption that the absorbed dose to an organ, sub-volume of an organ, tissue or cell can be related to the biological response or to the risk for stochastic effects, mainly the induction of cancer.

Dosimetry in nuclear medicine and RPT has predominantly been used for risk assessments (*1,80*). The high activities administrated can produce high absorbed doses to normal tissues that can cause adverse radiation damage. By estimating the absorbed dose to OARs, limits for administrated activity have been established to avoid serious side effects for patients. Often, the tolerance data of different organs comes from experiences in EBRT (*81,82*).

However, the same tools used for risk assessments, can be used to tailor the therapy to individual patients, optimizing treatment by administrating enough activity to cause maximum damage to the target volume while keeping the risks for side effects below tolerable limits. In EBRT, patient-specific dosimetry is an established part of treatment planning, and it is well-documented to improve therapy outcome (*83*). This is however not the case in RPT, where common practice is still to administrate fixed activities to all patients. There is however a growing collection of studies reporting correlation between absorbed dose and RPT therapy outcome (*1*).

The arguments for going from risk-limiting activities to patient-tailored treatment planning in RPT has been expressed for several decades, but still clinics struggle to implement patient dosimetry (*1,84,85*). Since many patient-specific parameters influence the resulting absorbed dose in both target and non-target volumes, the task at hand is very complex, and building robust methods have proved to be a challenge (*86*). However, efforts to coordinate and guide dosimetry development have been made, including the reports from ICRU on RPT (*1,84*).

One limiting factor is the lack of sensitivity and spatial resolution in quantitative in vivo imaging of therapeutic radiopharmaceuticals by PET and SPECT. This leads to big uncertainties in the measured activity in delineated volumes, and subsequently uncertainty in any absorbed dose calculation (*87*). However, it can still contribute to a more personalized treatment. For example, Sundlöv et al. measured activity in the kidneys after ^{177}Lu-DOTATATE administration with SPECT/CT and planar

scintigraphy to perform kidney dosimetry after each treatment cycle. The number of treatments could for a majority of patients be increased from the standard four by allowing a total BED up to 40 Gy (*57*).

In preclinical trials for new radiopharmaceuticals, dosimetry plays a vital role to evaluate the treatment response and the translatable potential from animal model to human (*12,31*). However, many trials are still performed without any dosimetry and only report administrated activities (*12*). As in clinical dosimetry, absorbed dose uncertainties can impact the interpretation of treatment outcome. But this should not be taken as a reason to omit dosimetry in the preclinical phase of radiopharmaceutical development. The EANM Radiobiology Working Group argues that preclinical models, both in vitro and in vivo, need standardized radiation transport models, to avoid dosimetry discrepancies (*88*). They also suggest standardizing reporting of dosimetry, dose-related effects, and radiobiological endpoints.

In vitro irradiations of cancer cell lines are used to evaluate the cell survival fraction (SF) for a given absorbed dose. SF investigated for varying absorbed doses is most often fit to the LQ-model, to estimate the radiosensitivity, expressed as the α and β parameters. When investigating the radiosensitivity of a cell line, the irradiation geometry must be considered to ensure correct estimate of the absorbed dose. For radiopharmaceuticals, its uptake, internalization and redistribution will affect the resulting absorbed dose to individual cells and cell nuclei. Similarly, irradiations with short range radiation for radiobiological studies can cause a large variance in experienced absorbed dose by cells in vitro. To consider this, small-scale or micro-dosimetry models need to be implemented, to correctly correlate the radiation response.

5.1 MIRD formalism

The MIRD formalism (*1,84,89*) is a standardized scheme for internal dosimetry of radioactive sources. In it, volumes in the body such as organs, tissues, or sub-volumes of these are considered target or source volumes. Source volumes containing radioactivity can contribute "cross-dose" to other volumes, then considered the target. The target volume can also be a source volume, contributing absorbed dose to both itself and other volumes. The cumulated activity in a source volume, $\tilde{A}$, is the time-integrated activity in that volume. Effectively, this equals the total number of disintegrations of the radionuclide over the time frame T_D considered.

The mean absorbed dose to a target volume r_t per cumulated activity in a source volume r_s, is referred to as the S factor:

$$S(r_t \leftarrow r_s) = \frac{\sum_i \Delta_i \phi_i(r_t \leftarrow r_s)}{m_t} \tag{5.1}$$

The S factor depends on the mean energy emitted per decay Δ_i, the absorbed fraction in the target volume $\phi_i(r_t \leftarrow r_s)$ for the *i*th radiation emitted from the source volume, and the mass m_t of the target volume. Then, the mean absorbed dose $D(r_t \leftarrow r_s, T_D)$ from a source volume r_s to a target volume r_t is given by:

$$D(r_t \leftarrow r_s, T_D) = \tilde{A}\left(r_s, T_D\right) S(r_t \leftarrow r_s) \tag{5.2}$$

The total mean absorbed dose $D(r_t, T_D)$ to the target volume is then the sum of the dose contribution from all considered source volumes:

$$D(r_t, T_D) = \sum_s \tilde{A}\left(r_s, T_D\right) S(r_t \leftarrow r_s) \tag{5.3}$$

By shifting perspective and considering all defined volumes as a target, the absorbed dose for all volumes of interest is calculated. Volumes are defined in each specific calculation, meaning the MIRD formalism can be applied at any scale, from whole organs to molecular structures. In the common clinical case, they are defined as organs or voxels, while in vitro they commonly refer to cells or cell organelles.

Calculated and simulated S-values for multiple radionuclides have been published for standardized human phantoms (*90*). These are models of average human bodies, and their internal volumes can be rescaled by weight. Similarly, mouse and rodent phantoms are available to calculate S-values for preclinical dosimetry (*91-94*). For individual dosimetry, a detailed patient or animal model, for example, segmented from a CT scan, can be implemented in a Monte Carlo simulation to simulate S-values and effectively the absorbed dose by assigning sources to specified volumes (*95-98*).

Clinically, the MIRD formalism can be implemented by measuring the internal activity with quantitative PET, SPECT, or planar imaging, preferably at several time points. Then, by fitting a model to the measured activity, the cumulated activity is calculated as the area under the curve (AUC) (*1,80*).

5.2 Small-scale and Microdosimetry

The MIRD formalism assumes homogenous activity distribution within source volumes and calculates the resulting mean absorbed dose to the target volume. If the source volumes are organs, tissues or other macroscopic structures then any heterogeny

of the absorbed dose due to heterogeneous activity distribution within the source volume is disregarded. There might be local "hot spots" where the absorbed dose is much higher than the mean and similarly "cold spots" where the reverse is true. For radionuclides emitting short-range radiation, most source volumes contribute absorbed dose mainly to themselves. Cross-dose between neighboring cells can still be possible, depending on the range. The macroscopic approach is then at risk of misinterpreting the relationship between activity uptake and the resulting biological response, as the deposited energy is averaged over a macroscopic volume when the absorbed dose is calculated.

To account for short-range and high LET, small-scale, microscopic, and nanoscopic dosimetry models can be implemented where the size of the source and target volumes is matched to the range of the emissions and activity distributions considered (*20,99,100*). Some of the relevant aspects that motivate the use of small-scale or microdosimetry are illustrated in Figure 5.1. Radiation with low LET and photons from an external beam will cause sparse ionizations (Figure 5.1 A), while high LET particles generate dense ionization tracks (Figure 5.1 B). The biological outcome of high LET is, therefore, dependent on the distribution of the tracks. A track through the cell nucleus can cause multiple DSBs, while only passing through the cytoplasm might not cause any DNA damage. The likelihood of a track through the nucleus can increase if the radionuclide becomes internalized inside the cell. A radioactive source can emit its radiation isotopically (Figure 5.1 C). If closer to the target (the cell nucleus), the probability of a track through the nucleus increases (Figure 5.1 D).

For alpha, beta, and Auger emitters, their short ranges lead to energy depositions close to the point of decay. Alpha particles emitted from radionuclides applied in or considered for RPT typically have a range of 20-100 micrometers, beta particles have ranges of a few millimeters, and Auger electrons of 2-500 nanometers (*20,100,101*). As the alpha range is comparable to the diameter of a few cells, local variation in radiopharmaceutical uptake can cause a large variation in absorbed dose on a microscopic scale. For targeted therapies, the radiopharmaceutical uptake in a tumor volume will depend on the expression and availability of the targeted epitope. For example, the expression might vary between cells inside a tumor. Also, due to limited penetration into the tumor, receptors expressed by cells deep inside the tumor might be unavailable for the radiopharmaceutical. A macroscopic dosimetry model will not differentiate between the two cases described in Figure 5.1 E and F, where the tumors have taken up equal amounts of activity, but it has been distributed only on the surface (E) or penetrated inside the tumor (F).

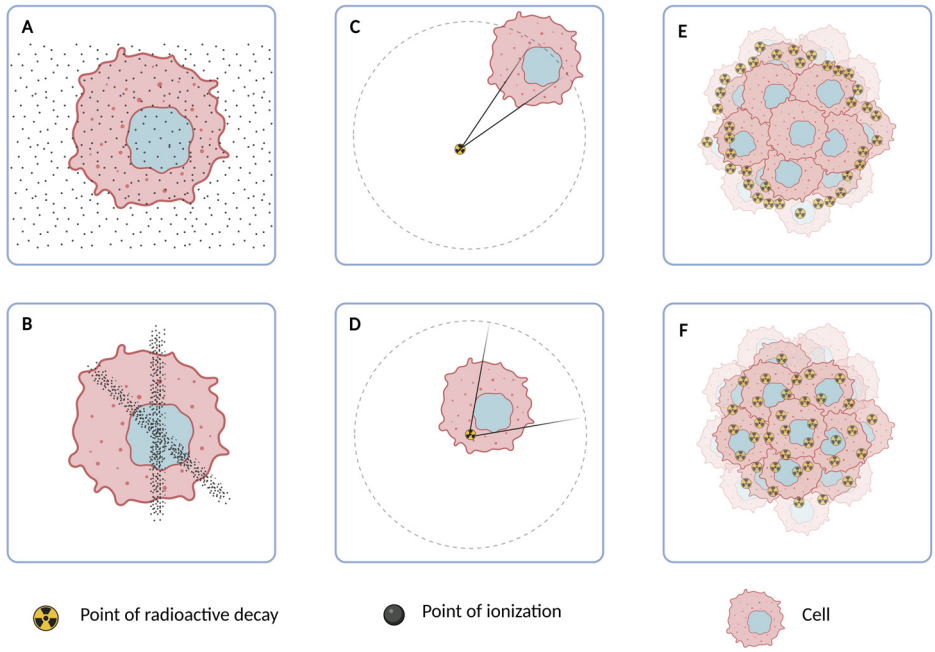

Figure 5.1. Aspects to consider for dosimetry of short-range and high LET radiation. Low LET and photon emission cause spares ionization (A). High LET particles, like alpha particles, cause dens tracks of ionization that have a high risk of causing DSBs if passing through a cell nucleus (B). Internalization of radionuclides can increase the likelihood of a track through the nucleus (C compared to internalized D). The intratumoral distribution of activity uptake can affect the biological response. Radiation emitted from activity taken up on the surface of the tumor (E), not penetrating to cells inside the tumor, is less likely to traverse a cell nucleus. In contrast, a homogenous intra-tumoral activity distribution increases the likelihood of all cells receiving particle tracks through their nuclei. Image (A) and (B) inspired by (*102*) and (C-F) inspired by (*10*) and (*80*). Created with BioRender.com.

The biological responses to radiation, including the induction of cancer, are processes of multiple events that happen at different spatial and temporal scales. Therefore, the interaction of radiation also needs to be considered on those scales. The absorbed dose (Eq. 2.2) is the quotient of the mean energy imparted ($d\bar{\varepsilon}$) by ionizing radiation to matter of mass dm, defined in a point (*1*). Still, it can be thought of as a macroscopic quantity. Since it calculates the mean absorbed dose in the macroscopic target volumes, it has not been sufficient to explain radiobiological effects such as mutations, chromosome aberrations, and carcinogenic risk for short-range radiation. However, considering the spatial distribution of energy depositions with the LET has helped interpret these effects (*99*). Furthermore, by calculating the relative biological effectiveness (RBE) between radiation of different qualities, a better understanding of the relevance of LET and the biological response has been achieved (*1*).

Damage to the DNA molecule that leads to cytotoxic DSBs results from interactions with small molecules. The width of a double-stranded DNA helix is approximately 2 nanometers (*16*). At this level, the energy depositions are mainly caused by secondary electrons set in motion by the radiation emitted from the radionuclide. These interactions are stochastic, not represented by the macroscopic mean absorbed dose. Therefore, a new stochastic quantity, *the specific energy,* z, was suggested. It can be calculated for a single energy deposition as the of the energy imparted, ε, in a volume of mass m (*89,99,100,103*).

$$z = \frac{\varepsilon}{m} \tag{5.4}$$

The variance of the multiple possible energy depositions is given by sampling the PDF of z, $f(z)$. Also, the mean specific energy $\bar{\varepsilon}$ equals the absorbed dose in the microscopic volume considered. In paper 3, we simulated the PDF of the specific energy in PC3 cell nuclei irradiated with alpha particles from an ^{241}Am source.

Many have used Monte Carlo and particle track structure codes to simulate the absorbed dose to cell models. The size and shape, the material composition, and distribution of the radionuclide affect the result. A common approach has been to simulate the cell and its nucleus as concentric spheres (*104-106*). If adherent, segmentation of the cell surface from fluorescent confocal microscopy images has been used to estimate the shape and size of cell nuclei (*107-109*). For Monte Carlo simulations on a sub-micro or nanoscale, such as models of the DNA molecule, regular condensed history physics codes are insufficient as the step length is too long. For this purpose, specific physics codes, such as the Geant4-DNA package, have been developed (*110*).

When performing cell irradiations with short-range particles from a radiopharmaceutical or an external source, a dosimetry model of sufficient detail is necessary (*111*). A few high LET particle tracks through the cell or cell nucleus are sufficient to generate cytotoxic effects. A single alpha particle passing through the cell nucleus can be enough to kill the cell (*41,112*). At these dose levels, the variance in particle tracks experienced per cell can be large, and many cells might not experience a single particle track through their nucleus. In contrast, when performing photon irradiations, thousands of primary photons are necessary to cause similar energy depositions compared to an alpha particle (*102*). Therefore, the variance is less relevant to consider.

When cells are irradiated in vitro from radionuclides by adding them to the cell medium, the simplest assumption is a homogenous distribution of radioactivity in the

medium. However, uptake on the cell surface and internalization into the cells changes the spatial and temporal activity distribution. For short-range radiation, this can mean a significant change in absorbed dose to the cell or cell organelles (*109*). In vitro experiments aimed to measure the radiosensitivity of a cell line to a radiopharmaceutical should therefore measure the activity uptake in relevant cell compartments, such as the cell nucleus, cytoplasm, and the cell membrane, and include these compartments in a small-scale dosimetry model, as exemplified by Ruigrok et al. (*113*). The EANM Radiobiology Working Group suggests requirements for reporting on cellular uptake kinetics, and compartments and morphology of small-scale dosimetry models should be defined (*88*).

5.3 Model of an in vitro alpha particle irradiator

For radiobiological experiments in vitro, solid alpha-emitting sources of long-lived radionuclides offer a simplified alternative to radiopharmaceuticals or specialized microbeam facilities (*112*). These preferably encapsulate the radioactivity in a durable metal shield with a thin foil window to allow alpha particles to escape. The use of these is often the result of in-house built setups to manage cell culture handling and sometimes dosimetry (*114*).

We used GATE to build a small-scale dosimetry model of an irradiation setup with an ^{241}Am source (half-life 432.2 years). The model included the alpha source, a cell well, and the cells at the bottom of the well exposed to the alpha particle fluence. This setup was implemented to simplify investigations with fluorescent biomarkers after alpha irradiation so that cells could be irradiated while growing on cover glasses at the bottom of a cell well. Before irradiation, the cell media had to be removed to enable alpha particles to reach the bottom of the well, otherwise stopped at the water surface. After irradiation, cells could be fixated and stained directly in the wells and then mounted on slides for fluorescence microscopy. This eliminated the need to trypsinize cells after irradiation and then mount the cells before imaging.

The setup differed from the original one built for this ^{241}Am source, for which a previous Monte Carlo dosimetry model had been made (*115*). Previously, cells were grown in well inserts on thin membranes. This proved challenging for the aims of paper 3 and resulted in a new design of the setup.

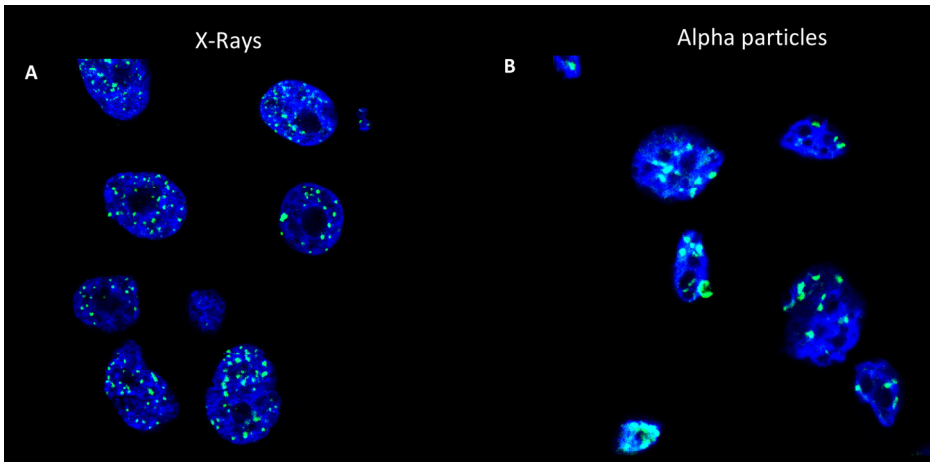

Figure 5.2 Comparison of γ-H2AX foci in DAPI stained PC3 cell nuclei after irradiation with x-rays (A) and alpha particles (B). Adapted from (*116*).

In paper 3, our model was used to compare the distribution of the simulated alpha particle tracks, or "hits," in PC3 cell nuclei to the induced number of γ-H2AX foci detected by immunofluorescent staining. We hypothesized that these distributions should be very similar, as the passage of an alpha particle through the cell nucleus is likely to induce DSBs (*112*). As investigated by Antonelli et al. and demonstrated in Figure 5.2, γ-H2AX foci caused by alpha particles are often larger than those induced by x-rays (*41*). They concluded that foci induced by alpha particles are likely clusters of DSB, while the smaller foci from x-rays are most probably individual DSB.

The outline of the study performed in paper 3 is summarized in Figure 5.3. The ^{241}Am source was used to irradiate PC3 cells on the bottom of cell wells by placing the alpha-emitting source on top of each well in a holder, centering the source window above the well (Figure 5.3 A). 30 minutes after irradiation cells were fixed and stained with DAPI, a blue-fluorescent DNA-stain that illuminates the cell nucleus, and with a primary anti-H2AX antibody targeting phosphorylated H2AX, followed by a secondary fluorophore-conjugated antibody targeting the primary antibody (Figure 5.3 B). The cell nuclei and foci were imaged on a confocal fluorescence microscope (Figure 5.3 C). By segmenting the DAPI fluorescent signal from confocal z-stack volumes of the imaged cell nuclei, 3D mesh volumes were generated that could be imported into the GATE simulation environment (Figure 5.3 D).

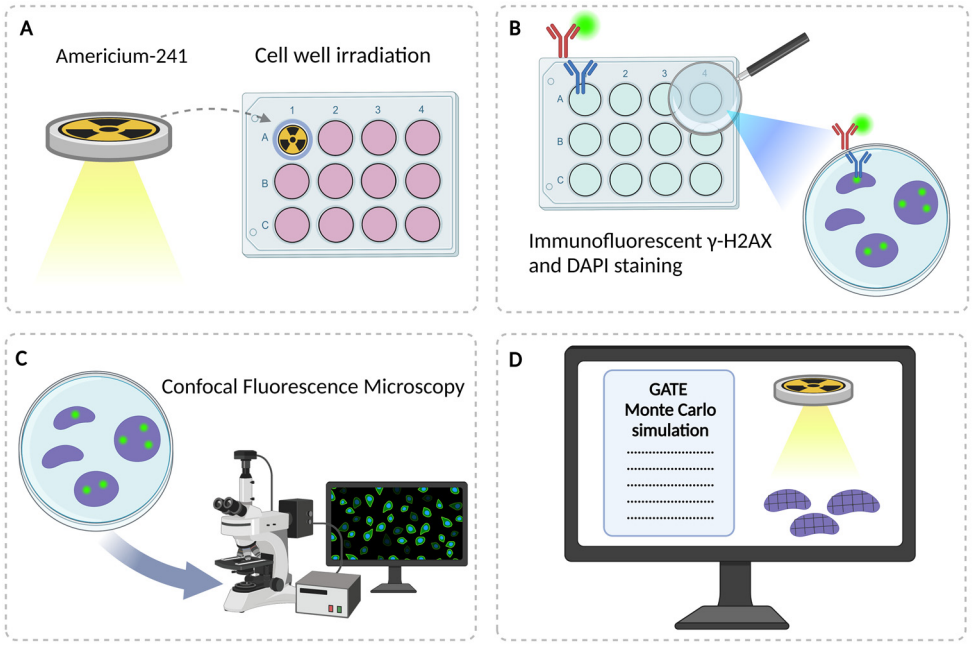

Figure 5.3 Project overview. Cells grown on a cover glass at the bottom of cell wells were irradiated with an alpha-emitting ^{241}Am source by placing it on top of the well (A). Irradiated cells were fixated and stained with DAPI, primary anti-γH2AX antibody, and secondary fluorescent secondary antibody (B). γ-H2AX foci and DAPI signal were imaged on a confocal fluorescent microscope (C). Segmented DAPI cell nucleus signal included in Monte Carlo dosimetry simulation (D). Created with BioRender.com.

Examples of two segmented PC3 cell nuclei are shown in Figure 5.4 A. For comparison, elliptical cylinders were also simulated as cell nuclei phantoms (Figure 5.4 B). To generate these, the major axis lengths of the ellipses were based on the distribution of the major axis length measured from central plane images of the DAPI signal (Figure 5.4 C), generating a representative distribution of cell nuclei sizes in the simulation.

Single-plane images at the center of the cell nuclei were used to detect γ-H2AX foci by image segmentation. As exemplified in Figure 5.5, detected foci were divided into small (red) and large (green) foci.

Since naturally occurring background foci tended to be small, and alpha particle-induced foci tended to be large, small foci were excluded from the analysis. To generate the radiation-induced foci (RIF) distribution, the detected RIF distribution was deconvolved by the detected foci distribution in sham-irradiated cells.

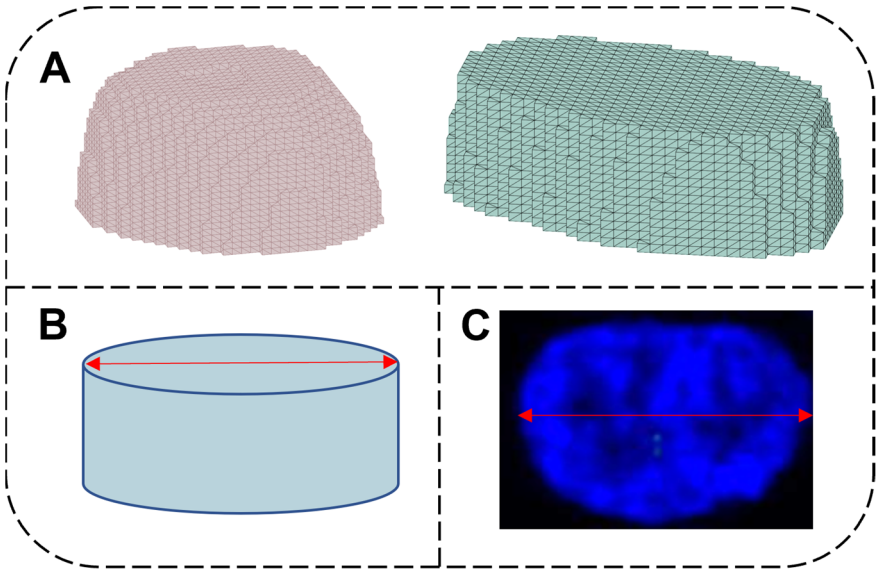

Figure 5.4 Segmented PC3 cell nuclei from confocal microscopy z-stack of DAPI signal (A and B). The generated mesh volumes were used as cell nuclei phantoms in the GATE simulation model of the alpha irradiation set-up. For comparison, elliptical cylinders were also used as cell nuclei phantoms in a simulation (C). The major axis lengths were measured in DAPI-stained PC3 cells to generate representative phantom sizes (D).

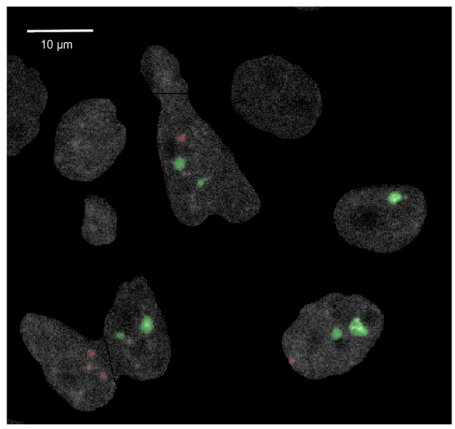

Figure 5.5 Segmentation of γ-H2AX foci from the fluorescent signal detected by confocal fluorescence microscopy. Foci were divided into small (red) and large (green) foci. Adapted from paper published in EJNMMI Physics (*116*).

The resulting comparison between alpha particle-induced and simulated RIFs is shown in Figure 5.6. The distribution overlap was very good for PC3 cells irradiated for 4, 8, and 12 minutes. At 4 minutes, the distributions approximately took the shape of a

Poisson distribution (Figure 5.6 A), but as irradiation time was increased, the distributions were better approximated by a Gaussian shape, as is the expected behavior of the distribution of the hits. Slight differences were generated by the two cell nuclei phantoms implemented. Still, the simpler elliptical cylinder phantom model seemed sufficiently detailed to estimate the RIF distribution as accurately as the more complex mesh volume model.

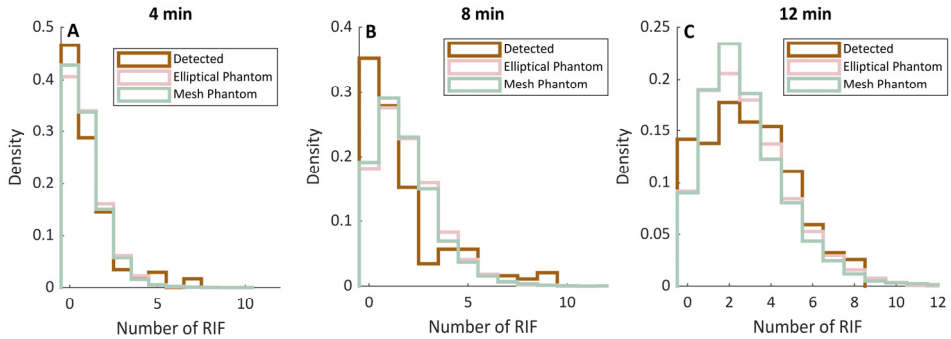

Figure 5.6 Comparison between detected and simulated γ-H2AX RIF distribution after 4, 8, and 12 minutes of irradiation. Adapted from paper published in EJNMMI Physics (*116*).

This study gave a clear example of how the biological response in alpha-irradiated cells demands a small-scale dosimetry model to be predicted. The γ-H2AX RIF distribution followed the distribution of alpha particles hitting the cell nuclei phantom volumes. This strengthens the hypothesis expressed by others that large RIFs are bundles of multiple DSBs induced along the track of an alpha particle. Therefore, when irradiating with alpha particles, the γ-H2AX RIF distribution seems to be a proxy for alpha particle tracks rather than the number of induced DSBs (41,108,112).

5.4 Tumor control probability

In tumor dosimetry, the aim is to relate the absorbed dose to the tumor treatment response. For that purpose, tumor control probability (TCP) models try to predict the outcome of radiopharmaceutical therapy. These are models adapted from experiences with EBRT for application in RPT, but they have yet to assemble the same experimental verification for their usefulness or accuracy as is available for EBRT. As pointed out by a recent review of TCP in targeted radionuclide therapy, TCP depends on the calculated absorbed dose (*117*). Consequently, if the dosimetry model lacks accuracy, so will the TCP model. Large uncertainties in radiopharmaceutical dosimetry

will propagate into the TCP models, making them only valuable when a robust dosimetry model, with a reasonable estimate of activity uptake and intra-tumoral distribution, spatial and temporal redistribution of activity, and tumor cell radiosensitivity, is established.

TCP models utilize the cell radiosensitivity, as evaluated by the LQ-model (equation 2.4), to calculate the cumulated probability that a population of cells will survive (or, invertedly, die). From the SF, the survival portion, SP_i, for the portion i of the cell population who have received the absorbed dose D_i is calculated. In paper 4, we used an adapted form of the LQ-model only considering the α parameter for the radiosensitivity. This has shown to result in a reasonably good fit for radiosensitivity to alpha particles and other high LET particles (*118*). Hence, the SP_i becomes:

$$SP_i = e^{-(\alpha * D_i)} \tag{5.5}$$

The TCP, defined as the probability to kill all cells in a tumor, for all intervals i, weighted by the number of cells N_c in each interval receiving the absorbed dose D_i is then given by:

$$TCP = \prod_i (1 - SP_i)^{N_c} \tag{5.6}$$

In the idealized case of RPT, all cells have received the same absorbed dose and $i = 1$ for all cells. Equation 5.6 then becomes:

$$TCP = 1 - SF \tag{5.7}$$

However, as investigated in paper 4, the absorbed dose experienced by individual cells in a tumor treated with RPT can have a high variance and depends on the range of the emitted radiation and the intra-tumoral activity distribution. Usijärvi et al. simulated non-uniform activity distributions in tumors for several radionuclides emitting radiation of varying ranges. They modeled cells and cell nuclei as concentric spheres and found that the TCP depends on the tumoral distribution and the intra-cellular compartment in which the activity resided (*119*).

The TCP estimate depends on the radiosensitivity parameters applied. These are commonly established from in vitro cell irradiations. In preclinical tumor models, radiosensitivity for the same cell line xenografted to the animal model is preferred as input to the TCP calculations. However, the radiosensitivity in vitro might still not represent the in vivo cell population in the xenograft. This is because the tumor microenvironment affects the cells response to radiation (*120*). Further, patient tumors

are not monocultures but consist of multiple cell types with varying radiosensitivity. Also, tumor cells belong to different subpopulations, with varying mutations, for example, mutations affecting the ability to repair radiation-induced damage (*121*), thereby affecting radiosensitivity.

Over an RPT cycle, a tumor can shrink by cell death, or grow by cell repopulation, if growth is faster than the treatment-induced cell death (*122*). Due to the low dose rate and longer half-lives of the radionuclides suitable for RPT, the absorbed dose is delivered over a time span where growth is necessary to consider. This can lead to a redistribution of the activity taken up by the tumor, alter the distance between regions of high and low uptake (hot and cold spots), and effectively introduce a range of uncertainty to models not considering these parameters. Preferably, more than one time point should be investigated post-injection during a preclinical RPT trial to enable interpolating the activity distribution over time.

5.5 Intra-tumoral absorbed dose simulation

The limited spatial resolution in clinical in vivo imaging makes detecting heterogeneous activity uptake in tumors, normal tissues, and OARs challenging. For alpha emitters, this is an even bigger challenge. However, some alpha emitters, such as ^{227}Th and ^{223}Ra, have gamma emissions that are detectable and can be utilized for activity quantification for internal dosimetry (*21,123*).

With autoradiography, the internal distribution of a radionuclide can be measured with a much higher spatial resolution compared to what is possible with in vivo PET and SPECT imaging (*124*). Thin cryosections of tumor or other dissected tissues mounted on slides are scanned to detect the spatial activity distribution. The spatial resolution depends on the energy of the detected emission and therefore differs between radionuclides. For example, the digital autoradiography (DAR) system utilized in paper 4 has an intrinsic spatial resolution of 50 µm (*125*), but the effective spatial resolution must be investigated for the radionuclide in question. Preclinical trials with xenografted animal models can explore this important dosimetry parameter unavailable in the clinical context. Solid tumors carried by xenografted mouse models have diameters in the order of one to a few centimeters. Using the activity quantification from autoradiography as input to dosimetry calculations offers an opportunity to investigate the resulting variance in absorbed dose.

Örbom et al. used DAR to investigate the distribution of ^{177}Lu-labeled monoclonal antibodies targeting colon carcinoma in a rat model (*126*). They illustrated the varying

intra-tumoral dose rate, spatially and temporally, up to 7 days post-injection. In a different study, the same group utilized the same DAR system and showed how the chelate-to-antibody molar ratio in the labeling process affected the intra-tumoral distribution of ^{177}Lu activity (*127*). Bäck et al. developed the alpha camera, a high-resolution system to detect alpha emitters in tissue sections (*128*). This was later utilized by Chouin et al. to detect ^{211}At in micro-metastases from a murine model and to calculate the resulting absorbed dose (*129*).

In paper 4, we measured the intra-tumoral ^{177}Lu uptake in LNCaP xenografts from mice injected with [^{177}Lu]Lu-PSMA-617 3 days post-injection. This was then used to describe the source in a GATE Monte Carlo dosimetry simulation. The outline of the study is shown in Figure 5.7. The TCP was calculated from simulated S-values and cell density maps generated by segmenting cell nuclei from hematoxylin and eosin (HE) stained adjacent tumor sections.

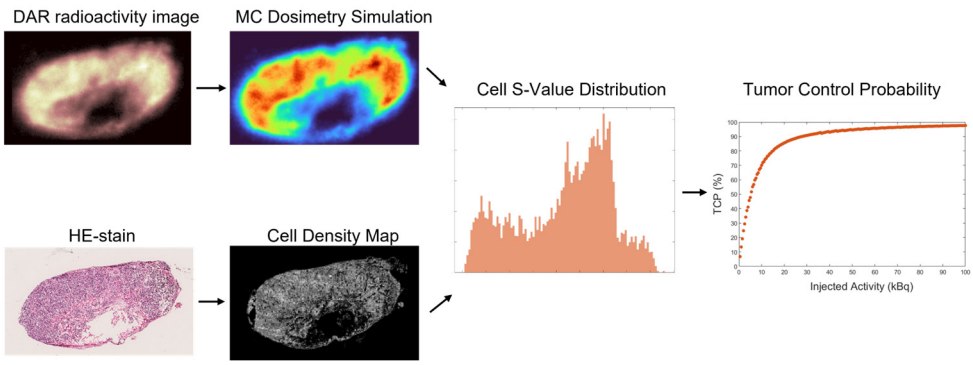

Figure 5.7 Outline of study in paper 4. DAR images are used as input in Monte Carlo dosimetry simulations. HE-stained tumor sections are used to generate cell density maps by image segmentation of cell nuclei. By combining the results, the cell S-value distributions were calculated and followingly the TCP as a function of injected activity.

In a previous study by our group, high-resolution DAR was used to image the heterogenous intra-tumoral uptake of ^{177}Lu in LNCaP xenografts in a mouse model treated with a ^{177}Lu-labelled monoclonal antibody targeting the human kallikrein 2 antigen, expressed in prostate cancers of all stages and in several prostate cancer cell lines. The study calculated the varying absorbed dose rate and the cumulative relative absorbed dose by considering the voxels within the tumor borders of the DAR images (*130*). In study 4, we compare the use of voxels to instead consider the density of cells in the voxels. The distribution of cells inside a tumor volume can vary. For example, necrotic areas, often in central hypoxic parts of the tumor, usually have a lower uptake

during RPT (*126*). However, fewer proliferative cells reside in these areas, so high absorbed doses are probably unnecessary to achieve a high TCP.

In the simulations, each pixel in the DAR image was defined as a source voxel, with dimensions equal to the DAR image pixel size (50 µm x 50 µm) and the width of twice the range of the simulated radiation. The normalized intensity in each DAR image pixel was used to define the relative activity in the corresponding source voxel. The simulations were run for the beta emitters ^{177}Lu and ^{90}Y and the alpha emitter ^{225}Ac, assuming the activity distributions would be the same regardless of the radionuclide used for labeling. For the beta emitters, only primary beta emission was simulated, disregarding photon emissions. In both cases, the sources were described in GATE as histogram sources based on the beta energy spectrums shown in Figure 5.8 A. The decay chain of ^{225}Ac is shown in Figure 5.8 B. Four alpha particles in the decay chain were considered in the simulations, ^{225}Ac (5.8 MeV) and alpha emissions from the daughters ^{221}Fr (6.4 MeV), ^{217}At (7.1 MeV), and ^{213}Po (8.4 MeV). These energies were stated as a discrete spectrum source with equal probability for emission. Accordingly, all daughters were assumed to be immobile, remaining in the same source voxel as the mother.

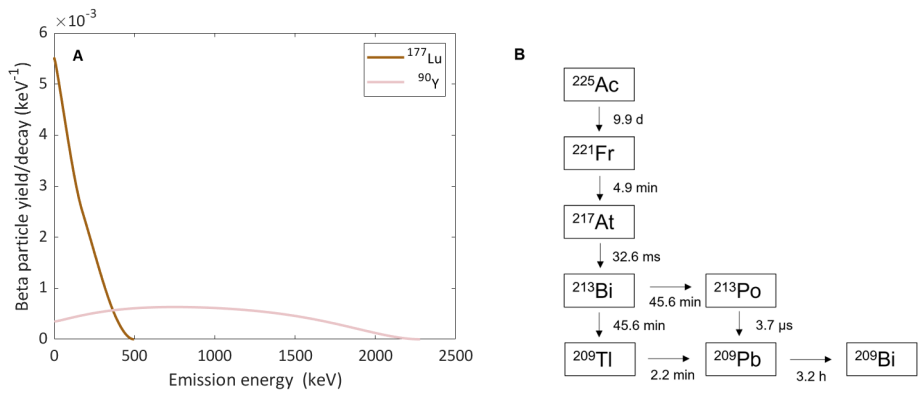

Figure 5.8 Beta energy spectrum for ^{177}Lu and ^{90}Y in (A) (*131,132*) and ^{225}Ac decay chain with half-lives given in (B). Adapted from submitted manuscrip.

A GATE Dose Actor was used to measure the absorbed dose from the simulation in a voxel volume overlapping the source volume. The voxels were 50 µm x 50 µm, and had a 10 µm width, to replicate the width of the original tumor section. To convert the detected absorbed dose, the number of interactions was scaled by the yield of the decay of the specific radionuclide simulated. This resulted in the absorbed dose rate per unit activity, also known as the S-value.

To illustrate how a peripheral activity uptake can affect the TCP, when activity is primarily taken up along the edge of the tumor, modified DAR images were generated by multiplying the original DAR images with a gaussian filter. The original DAR and resulting modified images used for source description in the simulations are shown in Figure 5.9 in the first two columns. Cell density maps for the three tumors are shown in the third column. The number of cells in a source voxel varied from 0 to 30. The original activity uptake (first column) and the cell density (third column) show great similarity for all three tumors, while activity has been removed from areas of high cell density in the modified images (second column).

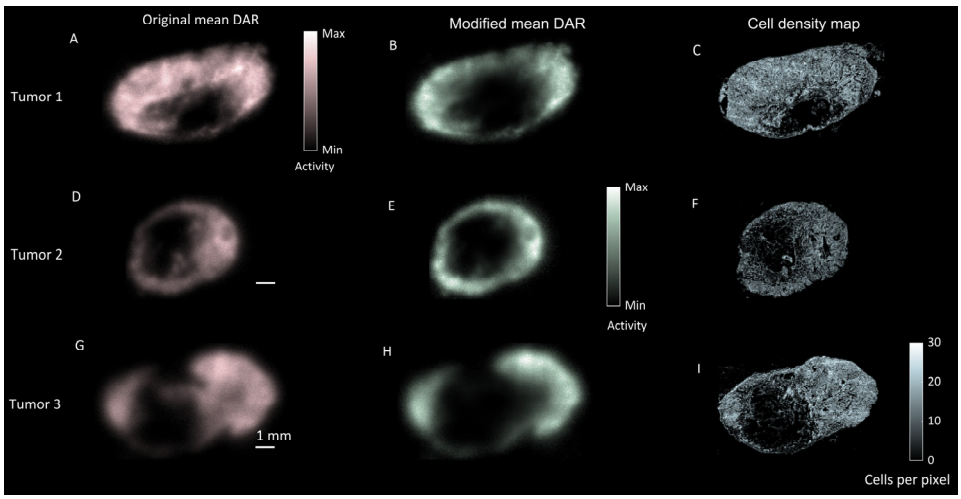

FIGURE 5.9 Resulting mean DAR image, modified DAR image after gauss filtering, and cell density map for tumors 1-3. The mean DAR image (A, D, and G) is the result of averaging eight sequential DAR sections after co-registration. The modified DAR images (B, E, and H) were generated by multiplying the mean DAR image with an oval gaussian filter, generating a hypothetical radioactivity distribution as if the tumor penetration was lower. The cell density map (C, F, and I) was produced from cell nucleus detection in HE-stained sections, created to relate the simulated absorbed dose in the same pixels/voxels to the number of cells, thereby generating the cell absorbed dose distribution. Adapted from submitted manuscript.

Figure 5.10 shows the resulting absorbed dose rate per activity unit, i.e., the S-value images for all investigated radionuclides in the three tumors from the sources described by the original DAR images. For each pixel in the cell density map, the number of cells was used to calculate the cell S-value distribution. As seen in the example histograms from Tumor 1 simulated with ^{225}Ac in Figure 5.11 A, the shape differed greatly from the voxel S-value distribution in Figure 5.11 B.

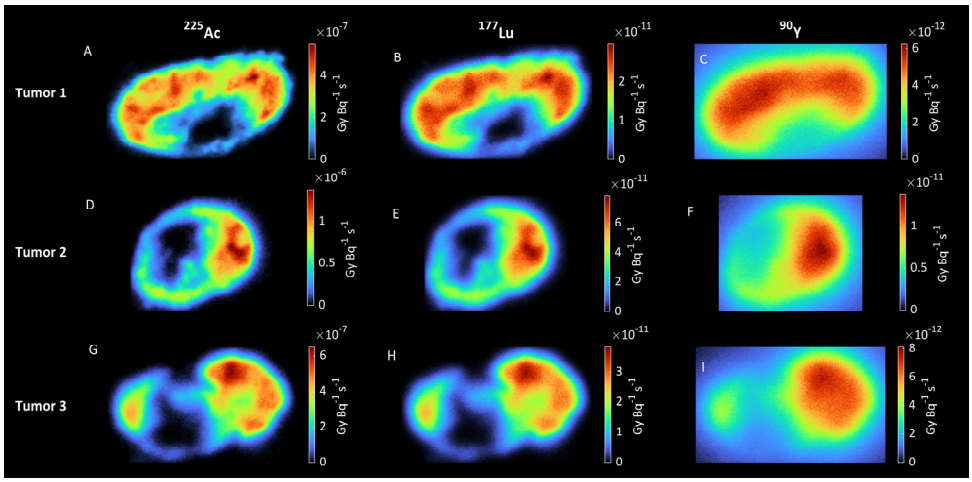

Figure 5.10 Simulated absorbed dose rate per unit activity, also known as the S-values in the MIRD formalism, in LNCaP tumor sections from tumors 1-3. Each pixel represents a voxel volume of 50x50x10 μm^3. Simulations were performed for the alpha or beta emissions of ^{225}Ac (A, D, and G), ^{177}Lu (B, E, and H), and ^{90}Y (C, E, and I). Image adapted from submitted manuscript.

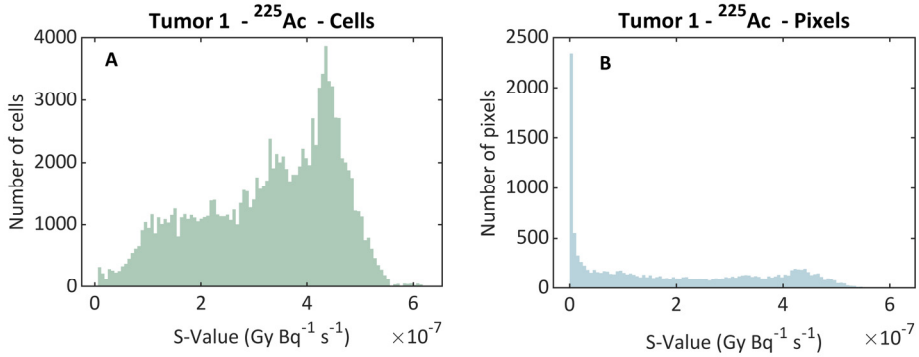

FIGURE 5.11. Cell S-value distribution for tumor 1 when treated with ^{225}Ac (A) and S-values of the pixel inside the tumor borders (B). Adapted from submitted manuscript.

For each S-value interval i, the absorbed dose D_i was calculated as the product of the cumulated activity $\tilde{A}$ and the S-value. By approximation, this can be rewritten as:

$$D_i = \tilde{A} \cdot S_i \approx 1.44 \cdot T_{\frac{1}{2}} \cdot A_0 \cdot S_i \tag{5.8}$$

where $T_{\frac{1}{2}}$ is the physical half-life and A_0 is the initial activity in the source volume. It was calculated as the product of the uptake U (%IA/g), the injected activity A_{inj} (Bq), and the tumor source volume V_{source} (g) considered in the simulation.

$$A_0 = U \cdot V_{source} \cdot A_{inj} \tag{5.9}$$

The average activity uptake was assumed to be 3.6 %IA/g of xenograft tissue, as was previously measured by our group (*28*), and the tissue density was assumed to be 1.0 g/cm^3.

With equation 5.6, the TCP for each distribution was calculated for a range of activities that are reasonable to inject into a mouse model. Also, by implementing a range of radiosensitivity, including those reported for LNCaP cells irradiated in vitro by Elgqvist et al. (*76*), the influence of radiosensitivity on TCP was investigated. The resulting TCP curves (Figure 5.12) allowed defining a range of activities probable to generate a desirable tumor response. In paper 4, we reported the injected activity necessary to reach a TCP of 90 % as a benchmark for a successful treatment.

The results clearly show how equal activity uptake can generate varying TCP due to the intra-tumoral distribution. The LNCaP xenografts investigated in this study showed a clear overlap between intra-tumoral activity distribution and cell density. Therefore, a modified example was generated to illustrate the effect of poor tumor penetration on the treatment response. For all investigated tumors and radionuclides, the modified activity distribution would require higher injected activities to reach 90 % TCP or could not be achieved in a few cases. The need for increased activity was highest for ^{225}Ac, were up to 4.5 times the injected activity would be necessary.

The importance of activity distribution has been investigated by others. Tamborino et al. evaluated the therapeutic efficacy of ^{177}Lu-DOTATATE by investigating the heterogenous intra-tumoral activity distribution and correlating it to γ-H2AX expression in tumor sections, finding a clear relationship (*133*). In our project, the change of radionuclide labeled to PSMA-617 was assumed not to affect the uptake or intra-tumoral distribution. Ruigrok et al. investigated the relative biological effectiveness in vitro between ^{177}Lu-PSMA-I&T and ^{225}Ac-PSMA-I&T by adding the radiopharmaceuticals to the cell medium (*113*). They found similar binding characteristics and performed a clonogenic assay to evaluate the radiosensitivity. They calculated the absorbed dose to the cell nucleus and the radiosensitivity for both radionuclides. In contrast to the radiosensitivity study of Elgqvist et al. used as input on alpha and beta particle radiosensitivity for LNCaP cells in paper 4 (*76*), this

approach takes the biokinetics of the radiopharmaceutical into account and considers the cell nucleus in its dosimetry model.

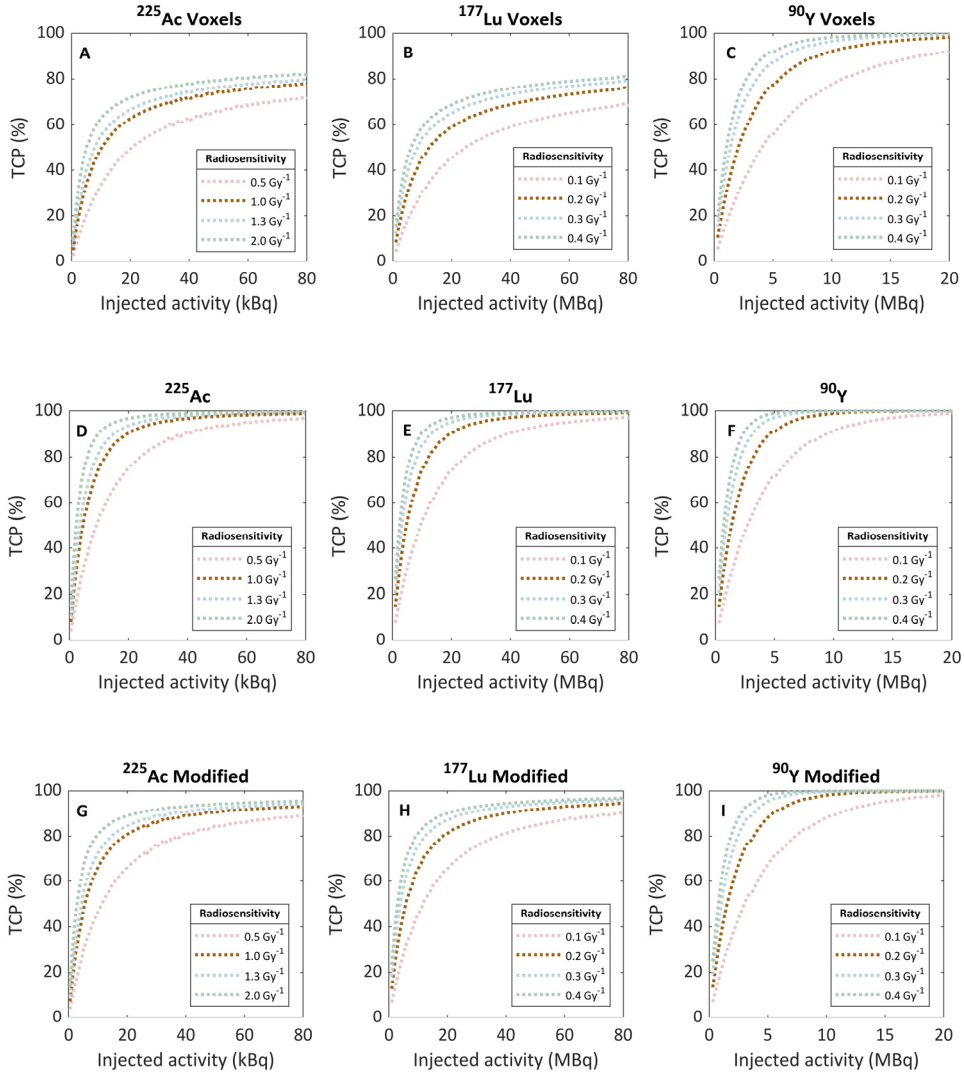

Figure 5.12 The TCP for Tumor 1 as a function of injected activity when considering the pixel s-value distribution (A)-(C), considering the cell S-value distribution (D)-(F) and considering cell S-value distribution from the modified activity distribution (G)-(I).

Interestingly, the radiosensitivity measured by Ruigrok et al. for ^{177}Lu-PSMA-I&T and ^{225}Ac-PSMA-I&T were 0.16 ± 0.01 Gy^{-1} and 0.67 ± 0.06 Gy^{-1} for PC3-PIP cells (a

modified version of PC3) treated in vitro. This is distinctly lower than the radiosensitivity detected for PC3 cells by Elgqvist et al. (*76*), 0.31 Gy^{-1} (95 % CI 0.28 – 0.34 Gy^{-1}) for beta and 1.9 Gy^{-1} (95 % CI 1.55-2.20 Gy^{-1}) for alpha particles. PC3 was, in turn, more radiosensitive than LNCaP cells in the Elgqvist study. Still, it raises the question of whether 1.3 Gy^{-1} might be too high an estimate of the radiosensitivity for the TCP calculations in paper 4. To tackle this uncertainty, we calculated the TCP for a radiosensitivity of 0.1, 0.2, 0.3, and 0.4 Gy^{-1} for beta particles and 0.5, 1, 1.3, and 2.0 Gy^{-1} for alpha particles. The activity necessary to reach a 90 % TCP for the three tumors investigated ranged from 10-55 kBq for ^{225}Ac, 10-56 MBq for ^{177}Lu, and 2.5-12 MBq for ^{90}Y. These results are of reasonable size for what is expected, based on absorbed doses not causing toxic effects but too general to guide us to an optimal injected activity.

The dosimetry model constructed in paper 4 makes no temporal considerations, as it is based on only one time point post-injection. However, it illustrated the resulting difference when considering the cell S-value distribution rather than the voxel distribution in TCP calculations. It could be expanded to consider temporal changes to the tumor volume and, if combined with specific radiosensitivity measurements performed as suggested by Ruigrok et al., the model would be tailored to the particular radiopharmaceutical and not just the type of radiation(*113*).

The GATE simulations offer a tool for further dosimetric investigations. An interesting approach for alpha emitters would be to investigate the possibility of calculating the TCP as a function of hits in the cell nucleus rather than the absorbed dose. Due to the limited spatial resolution of DAR, the simulations would have to be combined with a small-scale intra-tumoral dosimetry model, on par with the one created in paper 3.

6 Discussion and future directions

Targeting cell-specific receptors and delivering radionuclides emitting radiation to the tumor environment can offer curative treatments for cancers that today have a poor prognosis. RPT is a systemic form of radiotherapy, but unlike EBRT, many questions and issues regarding radiobiology and dosimetry remain unsolved. Most radiopharmaceutical therapies are administrated at given activity levels, not aimed to accomplish a certain absorbed dose to the target volume, not tailored to the individual patient, not taking tumor burden, radiosensitivity, receptor expression, or other parameters known to affect the absorbed dose and treatment outcome into account. The complexity of the biodistribution in multiple compartments of the body, the long retention times resulting in low dose rates, and the heterogenous activity distributions that cannot be measured accurately in vivo makes it a challenge.

For studies in vitro and in the preclinical phase of radiopharmaceutical development, dosimetry and study of radiobiological effects can be performed more efficiently and contribute to progress in the field. Treatment response needs to be correlated to the absorbed dose, and considerations must be taken to the short range of the radiation. The use of animal models is an ethical issue and studies performed without a dosimetry model risk generating inconclusive results without a fundamental explanation for the treatment response. To then ignore preclinical dosimetry is a wasted opportunity and an irresponsible use of resources.

Small-scale dosimetry models consider small volumes such as cells or the cell nuclei rather than tissues or organs. Due to the short range of alpha, beta, and Auger electrons, the spatial relationship between the emitter (the radionuclide or external source) and the target (the nucleus) is relevant to consider (*134*). In paper 3, we built a Monte Carlo model of an alpha-emitting source for cell in vitro irradiations. The model gave insight into the variance of alpha particle hits in the cell nuclei for a given irradiation time and absorbed dose. This was then related to the distribution of γ-H2AX foci detected in irradiated PC3 cells. For studies of radiobiological phenomena in vitro, a source used for external irradiations is a simpler, more general method than the direct use of radiopharmaceuticals, as this introduces the dependence on specific biokinetics. However, the LET of alpha particles irradiating cells from a solid source might differ

from alpha particles emitted from a radiopharmaceutical in vivo. This needs to be considered if the solid source is used to draw conclusions about a cell lines radiosensitivity to alpha emitters in the in vivo scenario. But without a detailed dosimetry model, none of this can be investigated.

Radiosensitivity has been investigated for various cancer cell lines (*135*). These results are utilized in the design of fractionation schedules for EBRT. However, less data is published for alpha particles, beta particles, and Auger electrons emitted by radionuclides. Comparisons may also be more complex as the assumptions of the underlying dosimetry models may differ significantly. Also, absorbed dose loses its fundamental meaning when a single alpha particle passing through a cell nucleus can be enough to kill the cell. Then, the exact energy deposited might not be the most relevant parameter to quantify, but rather the number of hits. At low absorbed doses, some cells might not have received a single hit, but the macroscopic quantity of absorbed dose does not reflect this.

In a macroscopic volume, such as a tumor, the absorbed dose to individual cells depends on the distribution of the activity. Measuring the activity uptake is therefore not enough to predict the treatment outcome, if the emitted radiation has a short range. Measuring the distribution of the activity on a small-scale or microscopic scale enable investigation of the absorbed dose variation among tumor cells and improves the tumor response prediction. As we suggest in paper 4, investigating the intra-tumoral absorbed dose distribution can be essential to understand why some therapies fail but others don't. We show, for three tumors, how the same activity uptake distributed across the tumor volume or focused on the tumor edge will generate very different absorbed dose distributions and TCP. This can be reflected in work previously published by our group (*127*), where changing the molar ratio when conjugating the humanized 5A10 (hu5A10) antibody to ^{111}In resulted in a more homogenous activity distribution inside xenografted tumors and an improved treatment response. This was visualized with DAR. In these kinds of studies, performing intra-tumoral dosimetry would enable a relevant correlation between absorbed dose and tumor response.

To advance preclinical trials of radiopharmaceuticals, the following workflow depicted in Figure 6.1 should be applied:

1. Perform in vitro cell irradiations with the radiopharmaceutical added to the cell media. Measure the activity in sub-cellular compartments and use it as input in a small-scale dosimetry model. Perform clonogenic assay to evaluate radiosensitivity.
2. Build a dosimetry model to calculate the absorbed dose from the activity measurements in cellular compartments.

3. Relate results from the clonogenic assay to the simulated absorbed dose and fit a survival model to evaluate the radiosensitivity.
4. Perform in vivo preclinical trials and collect intra-tumoral activity distribution by autoradiography.
5. Use autoradiography results to simulate the intra-tumoral absorbed dose heterogeneity.
6. Calculate the TCP or alternatively the necessary injected activity to reach a given TCP.

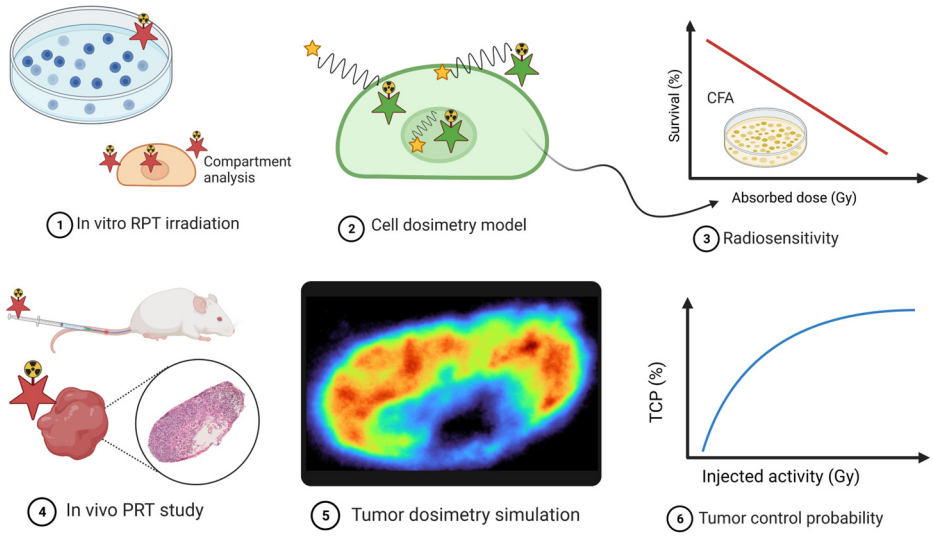

Figure 6.1 Suggested approach to utilize dosimetry in preclinical studies of new therapeutic radiopharmaceuticals. Created with BioRender.com.

A deeper understanding of how radiopharmaceuticals cause cell damage can be achieved through detailed dosimetry and will lay a stable foundation for more complex investigations of radiobiological phenomena, making the effect-size quantifiable. For radiobiological questions, intra-therapeutical imaging could also be an important tool. In papers 1 and 2, we investigated the limiting effect of a secondary radiation source in the preclinical PET FOV during imaging. This imitates performing PET imaging on an animal recently injected with ^{177}Lu for therapy. We saw a reduced resolution as a function of increased ^{177}Lu activity and a loss of the system's quantitative abilities, as the ^{177}Lu photons introduced dead-time in the PET system or contributed random coincidences by pile-up. We suggested a simple solution, using a shield to filter the lower energy photons emitted from ^{177}Lu. With GATE Monte Carlo simulations, we

could model the Genisys4 systems response and saw that the dead-time losses were the leading cause for signal loss. Furthermore, by simulating the shield, we could investigate the necessary shield thickness to gain a stable coincidence count rate over a relevant ^{177}Lu activity range to perform a longitudinal study.

Monte Carlo simulations can be further utilized for more specific questions at hand. We simulated a delayed coincidence rate to evaluate the introduction of random coincidences. We could have used the history of every ^{177}Lu gamma and ^{18}F annihilation photon to single out the "true" coincidences but only utilized this opportunity to distinguish between photons interacting in the detector volume. This could also have been used to investigate the properties and origin of the events contributing to dead-time losses and pile-ups.

Goorden et al. have shown the possibility of performing dual PET and SPECT by adding a pin-hole collimator to a preclinical PET system and applying two energy windows, one detecting low-energy photons (SPECT) and one detecting high-energy photons (PET) (*136*). It might be feasible that photons from ^{177}Lu could be detected simultaneously on a PET system if the shield was modified by introducing pinholes allowing a low fluence of photons to pass through. One way to investigate this and test the pin-hole design would be in a Monte Carlo simulation of a PET system, including a digitizer model to simulate the complete system response.

6.1 Conclusions

In this thesis, we have used experimental data to generate models that can help predict the outcome of future experiments, in preclinical PET-imaging, in in vitro cell irradiations and in preclinical RPT studies. As a final summary, these are the conclusions drawn from these experiences:

1. Intra-therapeutic imaging, as investigated in papers 1 and 2, can be useful for investigating the treatment response to RPT. Most promising is the opportunity to quantify DNA damage by γ-H2AX-PET at early time points after the therapeutic administration. For quantitative studies, it is necessary to investigate the ability of the preclinical PET system to produce a constant activity-to-coincidence signal for varying activities of the therapeutic radionuclide.
2. Small-scale dosimetry, as performed in paper 3, is necessary for in vitro irradiations with high LET radiation if the radiobiological parameter studied

is to be quantified as a function of energy deposited in a target volume, such as the cell nucleus.

3. Preclinical studies of RPT need to perform dosimetry that considers the intratumoral heterogeneity of the activity uptake to correlate the energy deposited to tumor response, as performed in paper 4. Evaluating TCP demands reliable radiosensitivity data.

4. The radiosensitivity should be evaluated for each radiopharmaceutical and cell line investigated in a preclinical trial. The uptake and internalization will affect the absorbed dose delivered to a cell as a function of activity. Therefore, a small-scale dosimetry model of the investigated cell line, like that in paper 3, will be necessary to investigate the absorbed dose to the cell nucleus.

7 Acknowledges

I am forever grateful for the support, help and guidance from all those who took part in the work with this thesis.

To my main supervisor *Sven-Erik Strand*. Thank you for taking me on a journey, by letting me find my way and by exploring what is possible with an open mind and a little bit of imagination.

To my co-supervisor *Magnus Dahlbom.* Thank you for sharing your knowledge, expertise, and warm hospitality at UCLA.

To my co-supervisor *Oskar Vilhelmsson Timmermand*. Thank you for all your ideas and new perspectives.

To my former supervisor *Johan Axelsson*. Thank you for helping me take the first steps, after the long walk, the shoes finally seem to fit!

To *Anders Örbom*, *Wahed Zedan*, *Mohamed Altai*, *Joanna Strand*, *Susan Evans-Axelsson*, *Pontus Kjellman,* and *Sofie Eriksson.* Thank you all for your help in the lab and for sharing your skills.

To my colleagues at the *Cyclotron unit, the Radionuclide therapy unit and the Department of clinical physiology, Lund*. Thank you all for offering a chance to lift my nose out of the books and look beyond the screen. You make nuclear medicine real.

To *Anna Stenvall, Johan Gustafsson and Elise Konradsson*. Thank you for sharing and caring for the lovely radiobiology lab exercise at the Medical radiation physics department. We made it fun!

To my dear family, my mother, father and brother, Elsa and Tyko, my extended family, old and new. You are my haven, my rock.

To Oskar, the wisest person I know. I love you.

8 References

1. Sgouros G, et al. Tumor Response to Radiopharmaceutical Therapies: The Knowns and the Unknowns. J Nucl Med. 2021;62:12S-22S.
2. Guidance for Preclinical Studies with Radiopharmaceuticals. Vienna: INTERNATIONAL ATOMIC ENERGY AGENCY; 2023.
3. Martinez NE, et al. Radium dial workers: back to the future. International Journal of Radiation Biology. 2022;98:750-768.
4. Jönsson B-A. The History of Nuclear Medicine. In: Ljungberg M, ed. Handbook of Nuclear Medicine and Molecular Imaging for Physicists: Instrumentation and Imaging Procedures, CRC Press; 2022:1-14.
5. Parker C, et al. Alpha emitter radium-223 and survival in metastatic prostate cancer. N Engl J Med. 2013;369:213-223.
6. Suominen MI, et al. Radium-223 Inhibits Osseous Prostate Cancer Growth by Dual Targeting of Cancer Cells and Bone Microenvironment in Mouse Models. Clin Cancer Res. 2017;23:4335-4346.
7. Mittra ES. Neuroendocrine Tumor Therapy: 177Lu-DOTATATE. American Journal of Roentgenology. 2018;211:278-285.
8. Fendler WP, et al. (177)Lu-PSMA Radioligand Therapy for Prostate Cancer. J Nucl Med. 2017;58:1196-1200.
9. Sathekge MM, et al. Global experience with PSMA-based alpha therapy in prostate cancer. European Journal of Nuclear Medicine and Molecular Imaging. 2021;49:30-46.
10. Kratochwil C, Haberkorn U, Giesel FL. 225Ac-PSMA-617 for Therapy of Prostate Cancer. Seminars in Nuclear Medicine. 2020;50:133-140.
11. Fallah J, et al. FDA Approval Summary: Lutetium Lu 177 Vipivotide Tetraxetan for Patients with Metastatic Castration-Resistant Prostate Cancer. Clinical Cancer Research. 2023:OF1-OF7.
12. Konijnenberg MW, de Jong M. Preclinical animal research on therapy dosimetry with dual isotopes. Eur J Nucl Med Mol Imaging. 2011;38 Suppl 1:S19-27.
13. Knoll GF. Radiation detection and measurement. 4. ed. ed: John Wiley; 2010.
14. Ljungberg M. Basics of Radiation Interactions in Matter. In: Ljungberg M, ed. Handbook of Nuclear Medicine and Molecular Imaging for Physicists: Instrumentation and Imaging Procedures, Volume I. Vol 1: CRC Press; 2022.

15. Nakamura N, et al. Radiation Effects on Human Heredity. Annual Review of Genetics. 2013;47:33-50.
16. Hall EJ, Giaccia AJ. Radiobiology for the radiologist: Wolters Kluwer Health; 2018.
17. Franken NA, et al. Clonogenic assay of cells in vitro. Nat Protoc. 2006;1:2315-2319.
18. Bodgi L, et al. Mathematical models of radiation action on living cells: From the target theory to the modern approaches. A historical and critical review. J Theor Biol. 2016;394:93-101.
19. McMahon SJ. The linear quadratic model: usage, interpretation and challenges. Phys Med Biol. 2018;64:01TR01.
20. Sgouros G, et al. MIRD Pamphlet No. 22 (abridged): radiobiology and dosimetry of alpha-particle emitters for targeted radionuclide therapy. J Nucl Med. 2010;51:311-328.
21. Sgouros G, et al. Imaging and dosimetry for alpha-particle emitter radiopharmaceutical therapy: improving radiopharmaceutical therapy by looking into the black box. Eur J Nucl Med Mol Imaging. 2021;49:18-29.
22. Mirabelli P, Coppola L, Salvatore M. Cancer Cell Lines Are Useful Model Systems for Medical Research. Cancers. 2019;11:1098.
23. Kaighn ME, et al. Prostate carcinoma: tissue culture cell lines. Natl Cancer Inst Monogr. 1978:17-21.
24. Horoszewicz JS, et al. The LNCaP cell line--a new model for studies on human prostatic carcinoma. Prog Clin Biol Res. 1980;37:115-132.
25. Huang R-X, Zhou P-K. DNA damage response signaling pathways and targets for radiotherapy sensitization in cancer. Signal Transduction and Targeted Therapy. 2020;5:60.
26. Olive KP, Tuveson DA. The Use of Targeted Mouse Models for Preclinical Testing of Novel Cancer Therapeutics. Clinical Cancer Research. 2006;12:5277-5287.
27. Dahlbom M. Preclinical Molecular Imaging Systems. In: Ljungberg M, ed. Handbook of Nuclear Medicine and Molecular Imaging for Physicists: Instrumentation and Imaging Procedures, Volume I: CRC Press; 2020.
28. Kristiansson A, et al. (177)Lu-PSMA-617 Therapy in Mice, with or without the Antioxidant alpha(1)-Microglobulin (A1M), Including Kidney Damage Assessment Using (99m)Tc-MAG3 Imaging. Biomolecules. 2021;11.
29. Costa P, et al. Translation of Radiopharmaceuticals: Mouse to Man. In: Ljungberg M, ed. Handbook of Nuclear Medicine and Molecular Imaging for Physicists: Radiopharmaceuticals and Clinical Applications, Volume III. Vol 3: CRC Press; 2022.
30. Vermeulen K, et al. Design and Challenges of Radiopharmaceuticals. Seminars in Nuclear Medicine. 2019;49:339-356.
31. Sgouros G, Hobbs RF, Abou DS. The role of preclinical models in radiopharmaceutical therapy. Am Soc Clin Oncol Educ Book. 2014:e121-125.

32. Anger HO. Use of a gamma-ray pinhole camera for in vivo studies. Nature. 1952;170:200-201.
33. Gear J. The Scintillation camera. In: Ljungberg M, ed. Handbook of Nuclear Medicine and Molecular Imaging for Physicists: Instrumentation and Imaging Procedures, Volume I. Vol 1: CRC Press; 2020.
34. Dahlbom M. Physics of PET and SPECT Imaging. 1st ed. ed. Boca Raton: Taylor & Francis Group; 2017.
35. Adler SS, Seidel J, Choyke PL. Advances in Preclinical PET. Seminars in Nuclear Medicine. 2022;52:382-402.
36. Reader AJ. Principles of Iterative Reconstruction for Emission Tomography. In: Ljungberg M, ed. Handbook of Nuclear Medicine and Molecular Imaging for Physicists: Instrumentation and Imaging Procedures. Vol 1: CRC Press; 2022.
37. Ng QK, et al. Total-body PET/CT - First Clinical Experiences and Future Perspectives. Semin Nucl Med. 2022;52:330-339.
38. Valente D, et al. Factors to Consider for the Correct Use of γH2AX in the Evaluation of DNA Double-Strand Breaks Damage Caused by Ionizing Radiation. Cancers (Basel). 2022;14.
39. Xu Y, Price BD. Chromatin dynamics and the repair of DNA double strand breaks. Cell Cycle. 2011;10:261-267.
40. Popp HD, et al. Immunofluorescence Microscopy of gammaH2AX and 53BP1 for Analyzing the Formation and Repair of DNA Double-strand Breaks. J Vis Exp. 2017.
41. Antonelli F, et al. Induction and Repair of DNA DSB as Revealed by H2AX Phosphorylation Foci in Human Fibroblasts Exposed to Low- and High-LET Radiation: Relationship with Early and Delayed Reproductive Cell Death. Radiat Res. 2015;183:417-431.
42. O'Neill E, Cornelissen B. Know thy tumour: Biomarkers to improve treatment of molecular radionuclide therapy. Nucl Med Biol. 2022;108-109:44-53.
43. Denoyer D, et al. Analysis of ^{177}Lu-DOTA-Octreotate Therapy–Induced DNA Damage in Peripheral Blood Lymphocytes of Patients with Neuroendocrine Tumors. Journal of Nuclear Medicine. 2015;56:505-511.
44. Knight JC, Koustoulidou S, Cornelissen B. Imaging the DNA damage response with PET and SPECT. Eur J Nucl Med Mol Imaging. 2017;44:1065-1078.
45. Cornelissen B, et al. Imaging DNA damage in vivo using gammaH2AX-targeted immunoconjugates. Cancer Res. 2011;71:4539-4549.
46. Knight JC, et al. PET imaging of DNA damage using (89)Zr-labelled anti-gammaH2AX-TAT immunoconjugates. Eur J Nucl Med Mol Imaging. 2015;42:1707-1717.

47. Poty S, et al. ^{89}Zr-PET imaging of DNA double-strand breaks for the early monitoring of response following α- and β-particle radioimmunotherapy in a mouse model of pancreatic ductal adenocarcinoma. Theranostics. 2020;10:5802-5814.
48. O'Neill E, et al. Imaging DNA Damage Repair In Vivo After (177)Lu-DOTATATE Therapy. J Nucl Med. 2020;61:743-750.
49. Kenny L. The Use of Novel PET Tracers to Image Breast Cancer Biologic Processes Such as Proliferation, DNA Damage and Repair, and Angiogenesis. J Nucl Med. 2016;57 Suppl 1:89S-95S.
50. Rajendran JG, Krohn KA. F-18 fluoromisonidazole for imaging tumor hypoxia: imaging the microenvironment for personalized cancer therapy. Semin Nucl Med. 2015;45:151-162.
51. Fonti R, Conson M, Del Vecchio S. PET/CT in radiation oncology. Semin Oncol. 2019;46:202-209.
52. Stieb S, et al. Longitudinal PET imaging of tumor hypoxia during the course of radiotherapy. Eur J Nucl Med Mol Imaging. 2018;45:2201-2217.
53. Oxboel J, et al. Comparison of two new angiogenesis PET tracers 68Ga-NODAGA-E[c(RGDyK)]2 and (64)Cu-NODAGA-E[c(RGDyK)]2; in vivo imaging studies in human xenograft tumors. Nucl Med Biol. 2014;41:259-267.
54. Nguyen QD, Aboagye EO. Imaging the life and death of tumors in living subjects: Preclinical PET imaging of proliferation and apoptosis. Integr Biol (Camb). 2010;2:483-495.
55. Qin X, et al. Radionuclide imaging of apoptosis for clinical application. Eur J Nucl Med Mol Imaging. 2022;49:1345-1359.
56. Sundlov A, et al. Phase II trial demonstrates the efficacy and safety of individualized, dosimetry-based (177)Lu-DOTATATE treatment of NET patients. Eur J Nucl Med Mol Imaging. 2022;49:3830-3840.
57. Sundlov A, et al. Individualised (177)Lu-DOTATATE treatment of neuroendocrine tumours based on kidney dosimetry. Eur J Nucl Med Mol Imaging. 2017;44:1480-1489.
58. Gustafsson J, Sundlov A, Sjogreen Gleisner K. SPECT image segmentation for estimation of tumour volume and activity concentration in (177)Lu-DOTATATE radionuclide therapy. EJNMMI Res. 2017;7:18.
59. Stenvall A, et al. Relationships between uptake of [(68)Ga]Ga-DOTA-TATE and absorbed dose in [(177)Lu]Lu-DOTA-TATE therapy. EJNMMI Res. 2022;12:75.
60. Uribe C, Celler A. Dead-time Effects in Nuclear Medicine Imaging Studies. In: Ljungberg M, ed. Handbook of Nuclear Medicine and Molecular Imaging for Physicists: Instrumentation and Imaging Procedures, Volume I. Vol 1: CRC Press; 2020.

61. Chapman SE, et al. Dual tracer imaging of SPECT and PET probes in living mice using a sequential protocol. Am J Nucl Med Mol Imaging. 2012;2:405-414.
62. Bai B, et al. Performance comparison of GENISYS4 and microPET preclinical PET scanners. Paper presented at: 2012 IEEE Nuclear Science Symposium and Medical Imaging Conference Record (NSS/MIC); 27 Oct.-3 Nov. 2012, 2012.
63. Bao Q, et al. Performance Evaluation of the Inveon Dedicated PET Preclinical Tomograph Based on the NEMA NU-4 Standards. Journal of Nuclear Medicine. 2009;50:401-408.
64. Goertzen AL, et al. Simultaneous molecular and anatomical imaging of the mouse in vivo. Phys Med Biol. 2002;47:4315-4328.
65. Duatti A. Review on (99m)Tc radiopharmaceuticals with emphasis on new advancements. Nucl Med Biol. 2021;92:202-216.
66. Mellhammar E, et al. Counting Rate Characteristics and Image Distortion in Preclinical PET Imaging During Radiopharmaceutical Therapy. Journal of Nuclear Medicine. 2016;57:1964-1970.
67. Sarrut D, et al. A review of the use and potential of the GATE Monte Carlo simulation code for radiation therapy and dosimetry applications. Med Phys. 2014;41:064301.
68. Jan S, et al. GATE: a simulation toolkit for PET and SPECT. Phys Med Biol. 2004;49:4543-4561.
69. Allison J, et al. Geant4 developments and applications. IEEE Transactions on Nuclear Science. 2006;53:270-278.
70. Agostinelli S, et al. Geant4—a simulation toolkit. Nuclear Instruments and Methods in Physics Research Section A: Accelerators, Spectrometers, Detectors and Associated Equipment. 2003;506:250-303.
71. Sarrut D, Ljungberg M. Monte Carlo Simulation of Nuclear Medicine Imaging Systems In: Ljungberg M, ed. Handbook of Nuclear Medicine and Molecular Imaging for Physicists: Instrumentation and Imaging Procedures. Vol 1: CRC Press; 2022.
72. GATE documentation. Updated on February 01, 2023; https://opengate.readthedocs.io/en/latest/index.html.
73. Geant4 Physics Reference Manual. https://geant4-userdoc.web.cern.ch/UsersGuides/PhysicsReferenceManual/html/index.html. Accessed 23 february, 2023.
74. Hubbell JH. Review and history of photon cross section calculations. Phys Med Biol. 2006;51:R245-262.
75. Fernández- Varea JM. Monte Carlo Simulation of Photon and Electron Transport in Matter. In: Ljungberg M, ed. Handbook of Nuclear Medicine and Molecular Imaging for Physicists. Vol 2: CRC Press; 2022.

76. Elgqvist J, et al. Radiosensitivity of Prostate Cancer Cell Lines for Irradiation from Beta Particle-emitting Radionuclide (177)Lu Compared to Alpha Particles and Gamma Rays. Anticancer Res. 2016;36:103-109.
77. Muehllehner G. Positron camera with extended counting rate capability. J Nucl Med. 1975;16:653-657.
78. Spinks TJ, Shah SI. Effect of lead filters on the performance of a neuro-PET tomograph operated without septa. IEEE Transactions on Nuclear Science. 1993;40:1087-1091.
79. Mellhammar E, et al. Preserving Preclinical PET Quality During Intratherapeutic Imaging in Radionuclide Therapy with Rose Metal Shielding Reducing Photon Flux. Journal of Nuclear Medicine. 2019;60:710-715.
80. Speer TW. Targeted Radionuclide Therapy: Wolters Kluwer Health/Lippincott Williams & Wilkins; 2015.
81. Bentzen SM, et al. Quantitative Analyses of Normal Tissue Effects in the Clinic (QUANTEC): an introduction to the scientific issues. Int J Radiat Oncol Biol Phys. 2010;76:S3-9.
82. Emami B, et al. Tolerance of normal tissue to therapeutic irradiation. Int J Radiat Oncol Biol Phys. 1991;21:109-122.
83. Muirhead R. Image-Guided Radiotherapy - The Unsung Hero of Radiotherapy Development. Clin Oncol (R Coll Radiol). 2020;32:789-791.
84. Adelstein SJ, et al. ICRU REPORT 67, Absorbed-Dose Specification In Nuclear Medicine. Journal of the ICRU. 2002;2.
85. Sgouros G, Hobbs RF. Dosimetry for radiopharmaceutical therapy. Semin Nucl Med. 2014;44:172-178.
86. Pandit-Taskar N, et al. Dosimetry in Clinical Radiopharmaceutical Therapy of Cancer: Practicality Versus Perfection in Current Practice. Journal of Nuclear Medicine. 2021;62:60S-72S.
87. Graves SA, Hobbs RF. Dosimetry for Optimized, Personalized Radiopharmaceutical Therapy. Seminars in Radiation Oncology. 2021;31:37-44.
88. Group ERW, et al. An EANM position paper on advancing radiobiology for shaping the future of nuclear medicine. Eur J Nucl Med Mol Imaging. 2023;50:242-246.
89. Bolch WE, et al. MIRD Pamphlet No. 21: A Generalized Schema for Radiopharmaceutical Dosimetry—Standardization of Nomenclature. Journal of Nuclear Medicine. 2009;50:477-484.
90. Chauvin M, et al. OpenDose: Open-Access Resource for Nuclear Medicine Dosimetry. Journal of Nuclear Medicine. 2020;61:1514-1519.
91. Bitar A, et al. A voxel-based mouse for internal dose calculations using Monte Carlo simulations (MCNP). Phys Med Biol. 2007;52:1013-1025.
92. Keenan MA, et al. RADAR realistic animal model series for dose assessment. J Nucl Med. 2010;51:471-476.

93. Larsson E, et al. Monte Carlo calculations of absorbed doses in tumours using a modified MOBY mouse phantom for pre-clinical dosimetry studies. Acta Oncol. 2011;50:973-980.
94. Larsson E, et al. Mouse S-factors based on Monte Carlo simulations in the anatomical realistic Moby phantom for internal dosimetry. Cancer Biother Radiopharm. 2007;22:438-442.
95. Gupta A, et al. Preclinical voxel-based dosimetry through GATE Monte Carlo simulation using PET/CT imaging of mice. Phys Med Biol. 2019;64:095007.
96. Abdul Hadi MFR, et al. Utilizing 3D Slicer to incorporate tomographic images into GATE Monte Carlo simulation for personalized dosimetry in yttrium-90 radioembolization. Medical Physics. 2022;49:7742-7753.
97. Costa G, et al. Radioembolization Dosimetry with Total-Body ^{90}Y PET. Journal of Nuclear Medicine. 2022;63:1101-1107.
98. Pistone D, et al. Relevance of artefacts in 99mTc-MAA SPECT scans on pre-therapy patient-specific 90Y TARE internal dosimetry: a GATE Monte Carlo study. Physics in Medicine & Biology. 2022;67:115002.
99. Li WB, Hofmann W, Friedland W. Microdosimetry and nanodosimetry for internal emitters. Radiation Measurements. 2018;115:29-42.
100. Hofmann W, et al. Internal microdosimetry of alpha-emitting radionuclides. Radiat Environ Biophys. 2020;59:29-62.
101. Pirovano G, Wilson TC, Reiner T. Auger: The future of precision medicine. Nuclear Medicine and Biology. 2021;96-97:50-53.
102. Monte Carlo simulations of cell response to DNA damage of various complexities. https://zfbweb.zfb.fuw.edu.pl/index.php/portfolio-item/monte-carlo-simulations-of-cell-response-to-dna-damage-of-various-complexities/. Accessed 20 February20 February, 2023.
103. Tronchin S, et al. Dosimetry in targeted alpha therapy. A systematic review: current findings and what is needed. Phys Med Biol. 2022;67.
104. Vaziri B, et al. MIRD pamphlet No. 25: MIRDcell V2.0 software tool for dosimetric analysis of biologic response of multicellular populations. J Nucl Med. 2014;55:1557-1564.
105. Chouin N, et al. Evidence of extranuclear cell sensitivity to alpha-particle radiation using a microdosimetric model. I. Presentation and validation of a microdosimetric model. Radiat Res. 2009;171:657-663.
106. Chouin N, et al. Evidence of extranuclear cell sensitivity to alpha-particle radiation using a microdosimetric model. II. Application of the microdosimetric model to experimental results. Radiat Res. 2009;171:664-673.
107. Reijonen V, et al. Multicellular dosimetric chain for molecular radiotherapy exemplified with dose simulations on 3D cell spheroids. Phys Med. 2017;40:72-78.

108. Barberet P, et al. Monte-Carlo dosimetry on a realistic cell monolayer geometry exposed to alpha particles. Phys Med Biol. 2012;57:2189-2207.
109. Tamborino G, et al. Cellular dosimetry of [(177)Lu]Lu-DOTA-[Tyr(3)]octreotate radionuclide therapy: the impact of modeling assumptions on the correlation with in vitro cytotoxicity. EJNMMI Phys. 2020;7:8.
110. Incerti S, et al. Review of Geant4-DNA applications for micro and nanoscale simulations. Phys Med. 2016;32:1187-1200.
111. Sgouros G. Dosimetry, Radiobiology and Synthetic Lethality: Radiopharmaceutical Therapy (RPT) With Alpha-Particle-Emitters. Seminars in Nuclear Medicine. 2020;50:124-132.
112. Gonon G, et al. From Energy Deposition of Ionizing Radiation to Cell Damage Signaling: Benchmarking Simulations by Measured Yields of Initial DNA Damage after Ion Microbeam Irradiation. Radiat Res. 2019;191:566-584.
113. Ruigrok EAM, et al. In vitro dose effect relationships of actinium-225- and lutetium-177-labeled PSMA-I&T. Eur J Nucl Med Mol Imaging. 2022;49:3627-3638.
114. Al Darwish R, et al. Development of a transmission alpha particle dosimetry technique using A549 cells and a Ra-223 source for targeted alpha therapy. Med Phys. 2016;43:6145.
115. Nilsson J, et al. Cancer Cell Radiobiological Studies Using In-House-Developed alpha-Particle Irradiator. Cancer Biother Radiopharm. 2015;30:386-394.
116. Mellhammar E, et al. Small-scale dosimetry for alpha particle 241Am source cell irradiation and estimation of γ-H2AX foci distribution in prostate cancer cell line PC3. EJNMMI Physics. 2022;9:46.
117. Spoormans K, et al. A Review on Tumor Control Probability (TCP) and Preclinical Dosimetry in Targeted Radionuclide Therapy (TRT). Pharmaceutics. 2022;14:2007.
118. Nahum AE. Microdosimetry and radiocurability: modelling targeted therapy with beta-emitters. Phys Med Biol. 1996;41:1957-1972.
119. Uusijarvi H, Bernhardt P, Forssell-Aronsson E. Tumour control probability (TCP) for non-uniform activity distribution in radionuclide therapy. Phys Med Biol. 2008;53:4369-4381.
120. Prasetyanti PR, Medema JP. Intra-tumor heterogeneity from a cancer stem cell perspective. Molecular Cancer. 2017;16:41.
121. Olivares-Urbano MA, et al. CSC Radioresistance: A Therapeutic Challenge to Improve Radiotherapy Effectiveness in Cancer. Cells. 2020;9:1651.
122. Vilhelmsson-Timmermand O, et al. Preclinical efficacy of hK2 targeted [^{177}Lu]hu11B6 for prostate cancer theranostics. Theranostics. 2019;9:2129-2142.
123. Larsson E, et al. Feasibility of Thorium-227/Radium-223 Gamma-Camera Imaging During Radionuclide Therapy. Cancer Biother Radiopharm. 2020;35:540-548.

124. Orbom A, Miller BW, Bäck T. Beta and Alpha Particle Autoradiography. In: Ljungberg M, ed. Handbook of Nuclear Medicine and Molecular Imaging for Physicists: Instrumentation and Imaging Procedures: CRC Press/Balkema; 2021:563-587.
125. Orbom A, et al. Characterization of a double-sided silicon strip detector autoradiography system. Med Phys. 2015;42:575-584.
126. Orbom A, et al. The intratumoral distribution of radiolabeled 177Lu-BR96 monoclonal antibodies changes in relation to tumor histology over time in a syngeneic rat colon carcinoma model. J Nucl Med. 2013;54:1404-1410.
127. Vilhelmsson Timmermand O, et al. A Conjugation Strategy to Modulate Antigen Binding and FcRn Interaction Leads to Improved Tumor Targeting and Radioimmunotherapy Efficacy with an Antibody Targeting Prostate-Specific Antigen. Cancers (Basel). 2021;13.
128. Back T, Jacobsson L. The alpha-camera: a quantitative digital autoradiography technique using a charge-coupled device for ex vivo high-resolution bioimaging of alpha-particles. J Nucl Med. 2010;51:1616-1623.
129. Chouin N, et al. Ex vivo activity quantification in micrometastases at the cellular scale using the alpha-camera technique. J Nucl Med. 2013;54:1347-1353.
130. Vilhelmsson-Timmermand O, et al. High resolution digital autoradiographic and dosimetric analysis of heterogeneous radioactivity distribution in xenografted prostate tumors. Med Phys. 2016;43:6632.
131. Mougeot X. Towards high-precision calculation of electron capture decays. Appl Radiat Isot. 2019;154:108884.
132. Mougeot X. Erratum: Reliability of usual assumptions in the calculation of beta and neutrino spectra [Phys. Rev. C 91, 055504 (2015)]. Physical Review C. 2015;92:059902.
133. Tamborino G, et al. Dosimetric Evaluation of the Effect of Receptor Heterogeneity on the Therapeutic Efficacy of Peptide Receptor Radionuclide Therapy: Correlation with DNA Damage Induction and In Vivo Survival. J Nucl Med. 2022;63:100-107.
134. Roeske JC, et al. Small-Scale Dosimetry: Challenges and Future Directions. Seminars in Nuclear Medicine. 2008;38:367-383.
135. van Leeuwen CM, et al. The alfa and beta of tumours: a review of parameters of the linear-quadratic model, derived from clinical radiotherapy studies. Radiat Oncol. 2018;13:96.
136. Goorden MC, et al. VECTor: A Preclinical Imaging System for Simultaneous Submillimeter SPECT and PET. Journal of Nuclear Medicine. 2013;54:306-312.

Printed by Media-Tryck, Lund 2023 NORDIC SWAN ECOLABEL 3041 0903

Tools for the Advancement of Radiopharmaceutical Therapy

Radiopharmaceutical therapy is used to treat cancers and other diseases with radiolabeled pharmaceuticals. The treatment targets specific cells, and the emitted ionizing radiation cause cytotoxic damage. Preclinical in vitro and in vivo experiments with radiopharmaceuticals and sources of ionizing radiation are performed to increase radiobiological knowledge and help optimize radiopharmaceutical therapy. Dosimetry is performed to estimate the absorbed dose from the energy deposited in the body, the tumor, or a single cell and is necessary to quantify the biological response to ionizing radiation. In addition, multiple types of molecular imaging, such as positron emission tomography, autoradiography, and fluorescence microscopy, can be used to investigate the treatment response.

LUND UNIVERSITY

FACULTY OF MEDICINE

Department of Clinical sciences, Lund

Lund University, Faculty of Medicine
Doctoral Dissertation Series 2023:46
ISBN 978-91-8021-386-8
ISSN 1652-8220